Journal of Cleaner Production 277 (2020) 122666

Contents lists available at ScienceDirect

Journal of Cleaner Production

journal homepage: www.elsevier.com/locate/jclepro

Analysis and prediction of gas turbine performance with evaporative cooling processes by developing a stage stacking algorithm

Mirhamed Salehi, Hamidreza Eivazi, Mojtaba Tahani*, Mehran Masdari

Faculty of New Sciences and Technologies, University of Tehran, Tehran, Iran

A R T I C L E I N F O

Article history:
Received 12 February 2020
Received in revised form
2 June 2020
Accepted 4 June 2020
Available online 22 July 2020

Handling Editor: Bin Chen

Keywords:
Gas turbine simulation
Efficiency improvement
Stage stacking
Evaporative cooling
Grey wolf optimization
Sensitivity analysis

A B S T R A C T

Water injection in stationary gas turbines is effective strategy for power augmentation and gas turbine efficiency improvement, in particular, at high ambient temperatures. In this study, a developed method for simulation of wet compression processes is introduced. This method is followed by the droplet evaporation analysis, aero-thermodynamic stage-stacking model, and a map zooming technique for evaluation the unknown parameters in the generalized performance curves by using grey wolf optimization (GWO) algorithm. The validity of the proposed algorithm is assessed through the comparison of the results with two experimental studies. The operating results are calculated for five different cities and 18 gas turbines organized in three classes. Moreover, a sensitivity analysis on the main input parameters is investigated with the use of variable importance (VI) analysis by constructing and training an artificial neural network. The results show that the variation of the output parameters is highly sensitive to the ambient temperature, relative humidity, and turbine inlet temperature (TIT). Results demonstrate that saturated fogging plus 1% overspray leads to a relative increase of 24.84% and 6.70% in net power output and thermal efficiency, respectively, at the corresponding ambient condition. It is observed that 23.94% of the increase in the inlet mass flow rate in this cooling approach is due to the injected water directly, where the compressor operating point is matched at a point with a higher inlet mass flow rate comparing to dry condition.

1. Introduction

During high ambient temperature periods, the ambient temperature increases and the compressor intake air density decreases. In this condition, the mass flow passing through the turbine reduces, and as a result the plant's efficiency and gained net power decreases. No doubt the gas turbine plays an important role in electrical power demand and peak load supply. The rising cost of energy and the increased gap between energy demand and supply have highlighted the need to develop energy conversion systems with improved thermodynamic efficiency and reduced emissions (Sahu and Sanjay, 2018; Sanjay, 2011). To increase the efficiency and gas cycle output power, the thermodynamic conditions of the inlet air and operation conditions must be changed. Various techniques including chillers (Mertens et al., 2015), fogging, and evaporative media cooler (Zurigat et al., 2006) are provided to reduce the inlet air temperature and increase the power output and efficiency of gas turbines. In addition, several studies were conducted for the liquefied natural gas (LNG) cold energy usage as inlet air cooling applications (Al-Ibrahim and Varnham, 2010). Inlet air cooling is a way to improve the efficiencies of gas turbines, and it is also one of the methods to vaporize LNG for the gas turbine power generation systems and the ambient air temperature is cooled in the LNG vaporizer. In evaporating cooling methods, the inlet air temperature decreases by water injection and density increases as a result. In the fogging inlet cooling, the nozzle arrays are placed as far away from the compressor inlet as possible. The wet compression spray nozzles were installed in the inlet duct downstream of the fogging nozzle arrays and the silencer. In some installation methods, the position of the nozzle arrays is considered between the air intake duct and expansion joint before the compressor. The nozzles are installed as close as to the compressor inlet to reduce water wastage prior to entry into the compressor. On the other hand, wet compression (overspray of water droplets inside the compressor), as a well-known evaporating method, has been widely used in recent years for power augmentation and gas turbine efficiency

* Corresponding author.
E-mail addresses: mir.salehi@ut.ac.ir (M. Salehi), hamid.eivazi@ut.ac.ir (H. Eivazi), m.tahani@ut.ac.ir (M. Tahani), m.masdari@ut.ac.ir (M. Masdari).

https://doi.org/10.1016/j.jclepro.2020.122666
0959-6526/

Nomenclature

Abbreviations

Gr	Grashof Number
Nu	Nusselt Number
Pr	Prandtl Number
sh	Sherwood Number
ANN	Artificial Neural Network
CET	Compressor Exit Temperature ($C\circ$)
CFD	Computational Fluid Dynamics
CIT	Compressor Inlet Temperature ($C\circ$)
GE	General Electric Co
GWO	Grey Wolf Optimization
HR	Heat Rate (kJ/kWh)
LCV	Low Calorific Value
LNG	Liquefied Natural Gas
MLP	Multilayer Perceptron
MSE	Mean Square Error
NIC	No Inlet Cooling
NOx	Nitrogen Oxides
OS	Overspray
PR	Pressure Ratio
RH	Relative Humidity
RPM	Revolutions per minute
RWI	Rate of Water Injection (kg/s)
SF	Shape Factor
SFo	Saturated Fogging
TET	Turbine Exit Temperature ($^{\circ}C$)
TIT	Turbine Inlet Temperature ($^{\circ}C$)
VI	Variable Importance

Greek Letters

η_p	Polytropic efficiency
Γ	Mass coefficient of diffusion
φ	Flow coefficient
ψ	Load coefficient

Other Symbols

Δm_d	Change in droplet mass (kg)
δ	Mass coefficient of diffusion (kg)
$\dot{m}$	Mass Flow Rate (kg/s)
$\dot{Q}_{lat.}$	Latent heat transfer rate (kW)
$\dot{W}$	Power (MW)
$\varphi_{\mathrm{evap.}}$	Mass transfer flux (kg/m^2 s)
ρ	Density (kg/m^3)
C_a	Axial velocity (m/s)
C_p	Specific heat at constant pressure (kJ/kg K)
C_w	Tangential velocity (m/s)
D_d	Droplet diameter (m)
$h_{conv.}$	Convection heat transfer coefficient (kW/m^2 K)
L_v	Latent heat of vaporization of water (kJ/kg)
M_a	Molar mass of air (kg/kmole)
m_d	Mass of droplet (kg)
P_{sl}	Saturated pressure (Pa)
P_v	Partial pressure of vapor (Pa)
R	Universal gas constant (J/mole K)
S_d	Droplet surface area ($^{\circ}C$)
t	Time (s)
T_a	Ambient air temperature ($^{\circ}C$)
T_d	Droplet temperature ($^{\circ}C$)
U	Blade tip velocity (m/s)

Superscripts

*	Dimensionless

Subscripts

c	Compressor
d	Droplet
f	Fuel
os	Overspray
ref	Reference
t	Turbine
D	Design condition

improvement. Wet compression increases the turbine capacity to fire more fuel in the combustor, without raising the firing temperature. Unlike the inlet fogging process, the wet compression can be operated even in the ambient conditions with high relative humidity. This method leads to an additional mass flow entry to the gas turbine comparing to the dry operating condition mainly due to the matching of the gas turbine components at a new operating point. The additional power gained by fogging is dependent upon the difference between the ambient dry bulb and wet bulb temperatures. However, the gains by wet compression are more consistent over a wider range of ambient conditions. In 1940ies water injection was applied to aero-engines (Hamrick and Beede, 1956). Sexton et al. (1998); Sexton and Sexton (2003) conducted a computational simulation based on enthalpy-entropy calculation and non-equilibrium analysis for droplet evaporation. The slip velocity was assumed zero in his model. Thermodynamic wet compression model was proposed by Hill (1963). He also conducted experiments on wet compression. This Model was developed by Zheng et al. (2002, 2003), and the water droplet evaporation time, droplet break-up time and the droplet sizes after the breakup was modeled. The evaporation model and droplet behavior in the compressor was developed by White and Meacock (2004, 2011). Polytropic efficiency assumed constant throughout the wet compression. They updated their model by applying quasi three-dimensional droplet motion and assuming slip velocity between droplet and air. Chaker et al. (2002) proposed a thermodynamic model based on non-equilibrium evaporation. The heat and mass transfer coefficients of droplet for natural and forced convection were modeled and described the effect of airflow velocity on fog droplet behavior. The model was applied for droplet evaporation simulation in the present study. A stage stacking model based on $\varphi - \psi$ stage modeling and generalized performance curves of compressors was first presented by Muir et al. (1989), and shape factor as a tuning unknown parameter was introduced by Cerri et al. (1993). Sanaye et al. (2006) studied the effect of wet compression on gas turbine performance based on the model given by Chaker et al. (2002), constant polytropic stage efficiency, and compressor stage modeling according to the work by Spina (2002) on the gas turbine performance prediction using compressor and turbine generalized performance curves. Their findings were compared with Fluent software. Wang and Khan (2008); Khan and Wang (2009) applied both non-equilibrium and equilibrium evaporation and employed a stage-stacking approach using two-dimensional compressor airfoil geometries with together equivalent polytropic efficiency. They also calculated the shape factor (SF) values to assess the potential improvement for using the generalized compressor performance curve to study wet compression. Inter-stage spray, including the analysis of the pre-heat and precool effect at each small stage of the overall compressor performance, has been investigated. Based on the proposed model, the local velocity diagram by allowing a stage-by-stage analysis of the fogging effect on airfoil aerodynamics and loading with known two-dimensional mean line rotor and stator geometries has been calculated. Khan and Wang (2006) developed a new model for burning low calorific value (LCV) fuels by using wet compression for a gas turbine system. The effects of overspray on the Gas turbine blades have been studied by Cataldi et al. (2006) and Matz et al. (2010) based on analysis of velocity triangles, non-equilibrium evaporation model, droplet wall interaction, splashing, film evaporation, load shift, and inter-stage analysis. Bhargava and Meher-Homji (2005) investigated the performance parameters such as compressor discharge temperature and pressure, air mass flow, heat rate, and net power output. The field data of inlet fogging and overspray for GE 9171E simple cycle gas turbine have been reported. Obermüller et al. (2012) presented a summary of the most important facts concerning wet compression and liquid-water compression in gas turbine engines. In their paper, the advantages and limitations of the different approaches have been discussed. Optimization algorithms have become popular in solving complicated industrial and engineering problems recently. Ehyaei et al. (2015) performed optimization of fog inlet air cooling system using genetic algorithm. Tahani et al. (2018) studied the effects of wet compression on V94.2 gas turbine performance using an analytical method based on droplet evaporation. In their paper, the turbine output work has been optimized by the metaheuristic algorithms cuckoo search and three variables including droplet diameter, amount of overspray and droplet temperature have been considered. Utamura et al. (1999) reported simple cycle GEF9E gas turbine experimental data. The results showed that injection of spray water of 1% to air mass ratio (fog and overspray) would increase power output by about 10% and thermal efficiency by 3%, respectively. Bagnoli et al. (2008) studied wet compression in terms of water injection, stage stacking scheme with flow and load relation, and shape factor. Roumeliotis and Mathioudakis (2004, 2010) studied the effect of water injection on the gas turbine and compressor off-design operation by applying the one-dimensional method. In their paper, they coupled compressor model to the engine model. Chaker and Mee (2015) analyzed the interaction between the atomized water droplets and the airflow within the confined geometry of inlet air ducts in order to select appropriate fog nozzles and optimize fog nozzle manifold locations in the inlet ducts. Liu et al. (2019) used computational fluid dynamics (CFD) model to simulate the effect of wet compression on a multistage axial subsonic compressor. They showed the performance of the compressor was improved with the overspray cooling method. The results indicated that the influence of pneumatic crushing on the water droplets below 20 μm could be ignored, and the effect of blade collision on water droplets above 5 μm should be considered in the wet compression conditions. Recently, an analytical model has been formulated and implemented by Mohan et al. (2019) in order to study the wet compression process. The results showed that wet compression process can significantly increase the energy savings of power generation cycle. The droplet diameter plays a key role in the erosion of compressor blades caused by tiny water droplets. When the droplet sizes increase, the risk of compressor blade erosion increases accordingly. The larger droplets travel at a lower velocity than smaller particles, and it leads to an impact on the leading-edge suction side of the moving blades (Mertens et al., 2015). Smaller enough sprayed droplet size can not only ensure the compressor performance of wet compression, but also avoid the erosion caused by water film accumulation (Kanbur et al., 2018). White and Meacock (2004) have pointed out that only droplets smaller than 5 μm have no effects on compressor blade and the no slip assumption is valid for this rang of droplet diameter. Chaker et al. (2003) showed the largest droplets, of the order of 50 μm, have a response time of less than 8 ms, while droplets of 10 μm have a response time of only about 0.3 ms. Khan and Wang (2008) showed droplets size distribution without considering breakup and coalescence in a range of 10–25 μm and the largest erosion takes place near the rotor trailing edge and stator leading edge. Producing small size droplet over the whole spray is one of the main goals of nozzle technology development. This work focuses on water injection systems which produce droplets with 10 μm mean sauter diameter. The nozzles generally valid with respect to the present technology, available on the market, and suitable for gas turbine applications.

Wet compression and inlet fogging, has been widely used in recent years for power augmentation, nitrogen oxides (NOx) declination, and gas turbine efficiency improvement. As a consequence, injection of water into the air leads to a reduction of polluting emissions, particularly nitrogen oxides (Hendricks et al., 2005). Novelo et al. (2019) have applied wet compression to reduce NOx emissions and enhance engine performance. The test on the single-shaft Artouste engine showed a reduction in compressor discharge temperature by up to 34 $^\circ C$ and a NOx decrease by 25%. Mapna group studied the effects of wet compression cooling technique on the MGT-70 machines for a few subject cities (MAPNA, 2018). Mee Industries Inc. pioneered gas turbine inlet fogging and wet compression technology and reported the improvement of gas turbine output from 10% to 25% anywhere in the world (MeeFog, 2015). Siemens reported power increase and the heat rate improvement up to 25 MW and up to 3% respectively (Siemens, 2013). More than 45 wet compression systems are implanted by Siemens energy on various frame types. Wet compression is applicable for the SGT5-2000E (V94.2), SGT6-2000E (V84.2), SGT6-3000E (W501D5A), SGT5-4000F (V94.3A), SGT6-4000F (V84.3A), and SGT6-5000F (W501F-FC+) gas turbines.

This study aims to improve the existing wet compression theory by introducing a developed method based on map zooming procedure for evaluation of the compressor stage map in the wet operating conditions with the consideration of the entropy-enthalpy changes due to the heat and mass transfer between the air flow and water droplets, and to overcome the uncertain selection of the shape factor proposed by Spina (2002). The developed thermodynamic model can be applied for prediction and diagnosis of gas turbines performance and compressor modeling. The results of the algorithm can be used for stability, performance optimization and condition monitoring studies. Variation of compressor inlet temperature (CIT), compressor exit temperature (CET), turbine inlet temperature (TIT), turbine exit temperature (TET), compressor power consumption, net power output, heat rate, fuel consumption, and combustion chamber are studied, and the results are discussed and evaluated for the gas turbines which have been reported in the works by Bhargava and Meher-Homji (2005) and Utamura et al. (1999). Moreover, the so-called variable importance (VI) method based on the learning of the mapping of the inputs to the outputs using artificial neural networks (ANNs) is implemented for sensitivity analysis of the wet compression process to the gas turbine input data. As a summary, the followings are the contribution of this paper in the field of inlet fogging and wet compression:

- Introducing a novel method for evaluation of the unknown parameters in the generalized performance curves by using grey wolf optimization (GWO) algorithm
- Introducing a novel aero-thermodynamic stage-stacking model for analyzing wet compression process

- Developing a component matching and performing the thermodynamic analysis of the combustion chamber and power turbine
- Estimating the effects of wet compression on the compressor stages and operating parameters
- Implementation of the variable importance method for sensitivity analysis of the wet compression process to the gas turbine input conditions
- Estimating the operating parameters for 18 gas turbines in three ranges of net power outputs

2. Analysis methodology

2.1. Droplet evaporation model

The vapor penetration occurs from the layer near droplet surface to the ambient air with relative humidity equal to 100% (Sanaye et al., 2006). The concentration difference between the layer and ambient air leads to evaporation. Since the utilized model is based on semi-one-dimension approach, response time refers to the time needed for droplets to reach the air flow velocity has been considered. Some assumptions validated by Chaker et al. (2002) have been used in the modeling.

1. As the response time is lower than 10 ms (Chaker et al., 2002; Cataldi et al., 2006) and droplets are very small (less than 30 μm), the relative velocity to the gas path flow has been assumed zero. Moreover, the forced convection occurs when there is a slip velocity between the gas path flow and the droplet, and since the response time quickly reaches zero, the natural convection is dominant and the forced convection can be neglected.
2. The heat transfer to a droplet is coupled with mass transfer.
3. Radiation heat transfer has been neglected in order to avoid equation complexity.
4. Droplet has been assumed spherical.
5. The saturated vapor layer has been assumed around the droplet.
6. The droplet and its environment have been assumed isolated with uniform temperature.

Computations were carried out in small time intervals by using the relations in the following. This trend will continue until evaporation of all droplets at the end of the duct. The rate of observed heat by droplet is equal the rate of the connection heat between the droplet and surrounding air latent heat. The thermal equilibrium will be:

$$\dot{Q} = \dot{Q}_{conv.} + \dot{Q}_{lat.}. \tag{1}$$

The rates transferred by thermal convection between droplet and the air is calculated from:

$$\dot{Q}_{conv.} = h_{conv.} \times S_d \times (T_a - T_d). \tag{2}$$

$h_{conv.}$ is the thermal convective coefficient and is derived from the Nusselt number, and for natural convection, the Nusselt number is a function of the thermal Grashof and Prandtl Numbers as follows:

$$Nu = 2 + 0.6\, Gr_t^{0.25} \times Pr^{0.33}, \tag{3}$$

$$\dot{Q}_{lat} = \frac{\Delta m_d\, Lv}{\Delta t}, \tag{4}$$

$$L_v = 1000 \times (2498 - 2.413 \times T_d), \tag{5}$$

$$\Delta m_d = -\Delta t \times S_d \times \Phi_{\text{evap.}}. \tag{6}$$

$\Phi_{\text{evap.}}$ is the mass flux. By considering all conditions and assuming the air near the droplet as a perfect gas finally the evaporative flux may be written as:

$$\Phi_{\text{evap.}} = \frac{M\, sh\, \Gamma}{R\, D} \times \left(\frac{P_s}{T_d} - \frac{P_v}{T_a} \right). \tag{7}$$

The energy stored in a droplet during time interval will be:

$$\dot{Q} = m_d\, C_p\, \frac{T_{d(t+\Delta t)} - T_{d(t)}}{\Delta t}. \tag{8}$$

By substituting the Eq. (1) ~ Eq. (7) in Eq. (8):

$$T_{d(t+\Delta t)} = T_{d(t)} + \frac{\Delta t \times S_d}{m_d \times C_p} \left[h_{conv.} \times (T_{a(t)} - T_{d(t)}) - L_v \Phi_{\text{evap.}} \right]. \tag{9}$$

The right-hand side of Eq. (9) is the difference between the heat transfer from air to droplet and the required energy for droplet evaporation, also left-hand side of this equation is the change in droplet internal energy in a time interval. For droplet diameter, mass balance relation has been taken into calculation as:

$$D_{t+\Delta t} = \left(D_t^3 - \frac{\Delta m_d \times 6}{\rho^* \pi} \right)^{\frac{1}{3}}. \tag{10}$$

For presence of n droplets with same diameters for each mass unit of air, the air temperature around the droplet can be calculated as below:

$$T_{a(t+\Delta t)} = T_{a(t)} + \frac{h_{conv.} \times S_d}{C_p} \left[T_{d(t+\Delta t)} - T_{a(t)} \right] \times \Delta t \times n. \tag{11}$$

The computational model for droplet evaporation was developed by Chaker et al. (2002). This iterative model stops when the air becomes saturated meaning the droplet evaporates completely. The rate of the evaporated mass can be calculated by:

$$dw = \frac{sh \times \delta \times M_v \times S_d}{D_d \times R} \times \left(\frac{P_{sl}}{T_d} - \frac{P_v}{T_a} \right) \times dt, \tag{12}$$

where D_d is droplet diameter, and R is universal gas constant. The Sherwood number can be shown as a function of the Schmit number and the Grashof number (Chaker et al., 2002). The P_{sl} is the saturated pressure and can be calculated from relations described in the work by Lee and Kesler (1975). P_v is the partial pressure of the vapor and M_v is the molar mass of air. δ is the mass coefficient of diffusions and can be obtained from Chaker et al. (2002). S_d is the exchange surface of the droplet with the surrounding air.

2.2. Matching

When the components are integrated into an engine, the range of possible operating conditions for each component is considerably reduced. The main purpose of the matching component algorithm is to find corresponding operating points on the characteristics of each component when the engine is running at a steady speed or in equilibrium (Saravanamuttoo et al., 2001). In this paper, component matching is performed together with the thermodynamic analysis of the combustion chamber and power turbine, and the equilibrium operation of the gas turbine engine is achieved by the proposed algorithm.

- Input the operation parameters, including atmospheric, ISO, and design condition.
- Estimating the mass flow rate because the value is unknown in the off-design operating condition at the beginning.
- Reading compressor map and performing compressor calculation (evaluating pressure ration outlet temperature).
- Perform combustor calculation by means of fixed TIT or fuel mass rate consumption.
- Reading turbine map and performing turbine calculations. (Analyzing motor parameters and determining turbine pressure ratio).
- By knowing the inlet temperature of the turbine, turbine pressure ratio, and the specific rotational speed, the corresponding point in the turbine characteristic map can be obtained. As a result, the mass flow rate is calculated.
- The conservation of mass matches between turbine and compressor, and this iterative algorithm is continued till it converges.
- By evaluating the mass flow rate in the matching algorithm and the rotational speed, the turbine efficiency can be obtained.

By considering the pressure ratio and turbine mass flow rate, the corresponding point in the turbine map can be addressed. If the assumed value matches the value taken from the map, it will be chosen as an equilibrium running point; otherwise, this trial and error calculations should be carried out for a large number of points in the compressor map in order to modify the procedure. Fig. 1 demonstrates the proposed computational algorithm for matching the overall operation of a single-shaft engine with a power turbine.

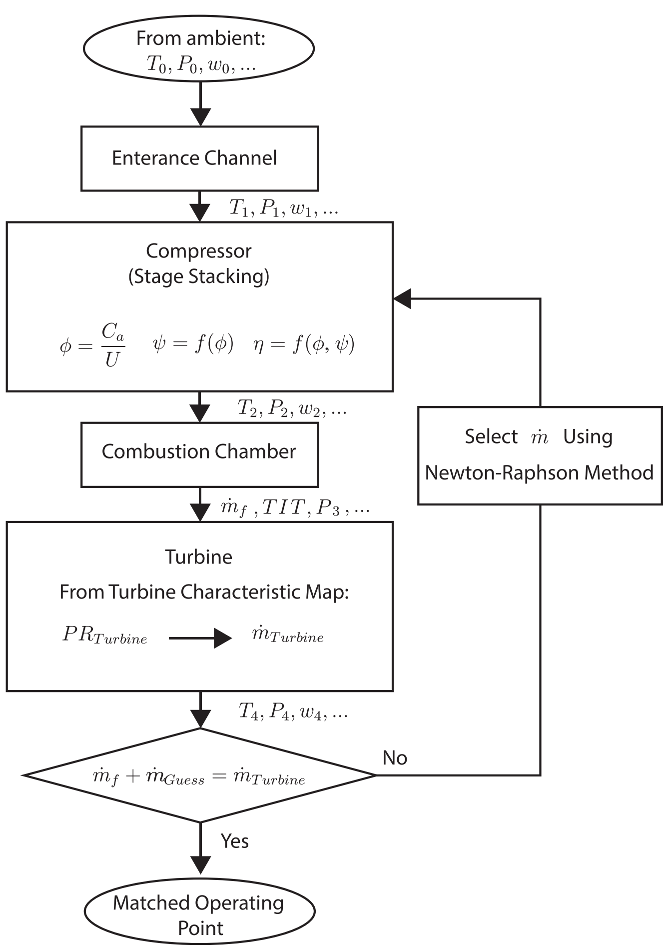

Fig. 1. The proposed computational algorithm for matching.

3. Compressor stage stacking

Compressor characteristic is an essential part of a gas turbine performance model. It's essential, for not only it gives researchers the opportunity to model the engine performance accurately, but also it could be an indicator to investigate the effect of variations in the compressor on the overall performance of the engine. Nevertheless, one of the major impediments to the development of the component-based engine models is the lack of available components data. Moreover, an accurate simulation of the wet compression process in the compressor of a gas turbine demands a stage stacking investigation. Several approaches were presented to overcome these issues. The main objective of the preponderance of previous works has been to study the effect of compressor deterioration on stage characteristics and overall compressor map. Muir et al. (1989) developed a general method for predicting the thermodynamic performance of variable geometry axial compressors, which has been applied to produce a gas turbine health monitoring system. The numerical procedure was based on finding specific values for the reference point of each stage. The generalized stage characteristic representations are then used to obtain the performance maps for each stage, and the stages are stacked to get the overall compressor characteristic map. Cerri et al. (1993) introduced stage shape factors (SF) for generalized pressure and efficiency curves of stages to acquire the best fitting between the calculated overall characteristic map and given data. Spina (2002) used the concepts of reference points and shape factors to model each compressor stage and propose Eq. (13). Implementing of the shape factor allows the representation of different types of compressor stages, included transonic and supersonic stages (negative SF values). Equation (13) presents the generalized relationship, which connects the values of flow coefficient φ and load coefficient ψ together:

$$\psi^* = \psi^*_{max} - \frac{(\psi^*_{max} - 1) \times \left(\varphi^*_{\psi_{max}} + \mathrm{SF} \times \left(\varphi^*_{\psi_{max}} - 1\right) - \varphi^*\right)^2}{\left(\varphi^*_{\psi_{max}} - SF \times \left(\varphi^*_{\psi_{max}} - 1\right) - 1\right)^2}. \tag{13}$$

Here, $\varphi = \frac{C_a}{U}$ and $\psi = \frac{\Delta h}{U^2}$. However, the selection and calculation of the shape factor is an uncertain process. It was shown that the considerable change in the shape factor from stage to stage and from case to case indicates the conventional practice of choosing a single shape factor to simulate a specific compressor may not be appropriate especially in fogging and overspray. Tsalavoutas et al. (1994) presented a method for accurate prediction of a multistage compressor map based on the combination of optimization techniques with the principles of stage stacking. The proposed method followed the principles of using generalized characteristic curves and normalized parameters φ/φ_{ref}, ψ/ψ_{ref} and η/η_{ref} where general characteristics are approximated by:

$$\psi \Big/ \psi_{ref} = \sum_{k=0}^{2} \alpha_k \left(\varphi \Big/ \varphi_{ref}\right)^k, \tag{14}$$

$$\eta \Big/ \eta_{ref} = \sum_{k=0}^{2} \beta_k \left(\varphi \Big/ \varphi_{ref}\right)^k. \tag{15}$$

Unknown parameters $\alpha_{0,\,1,\,2}$ and $\beta_{0,\,1,\,2}$ were calculated in an optimization process to provide an accurate prediction of overall compressor map. In the present study, Grey Wolf Optimization (GWO) algorithm (Mirjalili et al., 2014) is used for evaluating the unknown parameters in the generalized relationships. The objective is to minimize mean-squared error (MSE) of the calculated overall map through the stage stacking and the actual overall map defined as:

$$\mathrm{MSE} = \frac{1}{N}\sum_{i=1}^{N}\left(PR_{cal.} - PR_{map}\right)^2, \tag{16}$$

where N is the number of points extracted from the overall map and evaluated again through the stage stacking. Subscripts *cal.* and *map* show the calculated value and the original value from the map, respectively. Fig. 2 shows the computed mean MSE versus the number of iterations.

According to Cerri et al. (1993), the generalized relationship between ψ and φ may be written as Eq. (17) as follows:

$$\psi^* = a_{stage}\varphi^{*2} + b_{stage}\varphi^* + c_{stage}. \tag{17}$$

For $\varphi = \varphi_{ref}$, the generalized map should results in $\psi = \psi_{ref}$. Therefor, the generalized map should cross the point of ($\varphi^* = 1$, $\psi^* = 1$), which leads to the constrain of $a_{stage} + b_{stage} + c_{stage} = 1$. Consequently, there are 2 unknown parameters for load and flow coefficients relationship for each stage. Moreover, the generalized stage efficiency curve proposed by Howell and Bonham (1950) is used as the second generalized curve as:

$$\begin{aligned}
\eta^* &= 1 - \frac{1-\eta^*_{(\psi/\varphi)_{min}}}{\left[1-\left(\frac{\psi^*}{\varphi^*}\right)_{min}\right]^{3.5}}\left(1-\frac{\psi^*}{\varphi^*}\right)^{3.5}; \frac{\psi^*}{\varphi^*}\varepsilon\left[\left(\frac{\psi^*}{\varphi^*}\right)_{min}, 1\right] \\
\eta^* &= 1 - \frac{1-\eta^*_{(\psi/\varphi)_{max}}}{\left[\left(\frac{\psi^*}{\varphi^*}\right)_{max}-1\right]^{2}}\left(\frac{\psi^*}{\varphi^*}-1\right)^{2}; \frac{\psi^*}{\varphi^*}\varepsilon\left[1, \left(\frac{\psi^*}{\varphi^*}\right)_{max}\right].
\end{aligned} \tag{18}$$

The characteristic map of the last four stages is presented in Fig. 3. Now, with the calculation of $\varphi = \frac{C_a}{U}$, we can evaluate the outlet condition of each stage which is the inlet properties for the next stage. Axial velocity in each stage is calculated through a trial and error procedure based on velocity triangles formulations and stage characteristic map. From the generalized stage characteristic map, the enthalpy change can be evaluated as $\Delta h = \psi U^2$. Therefore, with knowing C_{w1} for the first stage, C_{w2} can be evaluated. At this point, axial velocity C_{a2} is guessed and is used for the calculation of velocity, static temperature and pressure, density, and mass flow rate. This procedure is followed to the convergence of the later calculated $\dot{m}$ to the $\dot{m}_{matching}$ from the matching loop. Fig. 4 depicts the algorithm which is developed for axial velocity calculation in each stage.

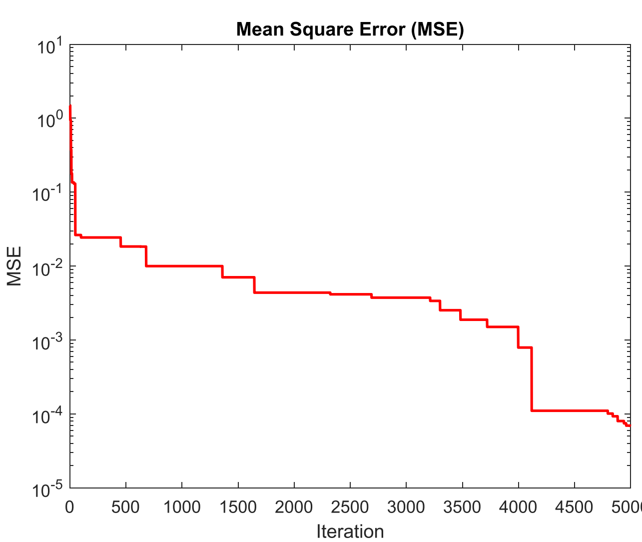

Fig. 2. Computed mean square error (MSE).

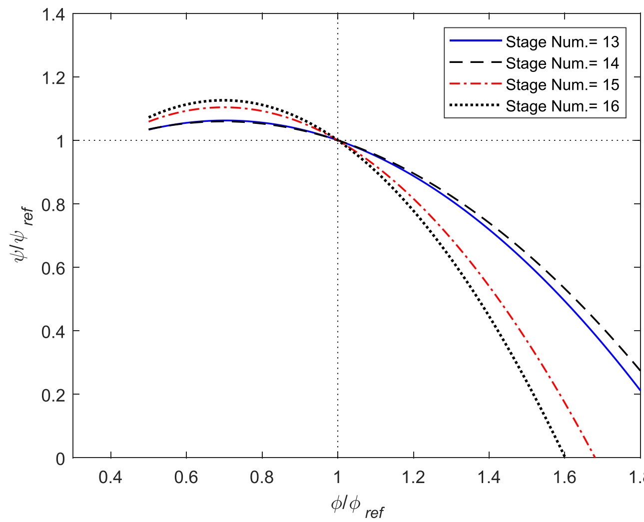

Fig. 3. Calculated stage characteristic map of the last four stages.

Fig. 5 shows the calculated and the experimental data points (Bhargava and Meher-Homji, 2005) on the scaled overall compressor characteristic map of GE9171E gas turbine.

The process of wet compression can be modeled through two steps. First, a polytrophic compression, and second, heat exchange between the water droplet and its surrounding air. A schematic of wet compression simulation method is illustrated in Fig. 6.

For the first step (compression) and with the implementation of the second low we have:

$$ds_{\mathrm{comp.}} = C_{pm}ln\frac{T_{2,\mathrm{comp.}}}{T_1} - Rln\frac{P_{2,\mathrm{comp.}}}{P_1}, \tag{19}$$

and:

$$\frac{P_{2,\mathrm{comp.}}}{P_1} = \left(\frac{T_{2,\mathrm{comp.}}}{T_1}\right)^{\frac{\eta_p C_{pm}}{R}}. \tag{20}$$

The subscript comp. shows the value related to the compression. For the second step (evaporation) entropy change can be calculated as:

$$ds_{\mathrm{evap.}} = -\frac{h_{fg}}{T_{\mathrm{Droplet}}}, \tag{21}$$

where subscript evap. shows the value related to the droplet evaporation. We can write:

$$ds = ds_{\mathrm{comp.}} + ds_{\mathrm{evap.}}, \tag{22}$$

$$\Delta h = \Delta h_{\mathrm{comp.}} + \Delta h_{\mathrm{evap.}}, \tag{23}$$

where $\Delta h_{\mathrm{comp.}} = \psi U^2$ and $\Delta h_{\mathrm{evap.}} = -h_{fg}$. From Eq. (22) and Eq.

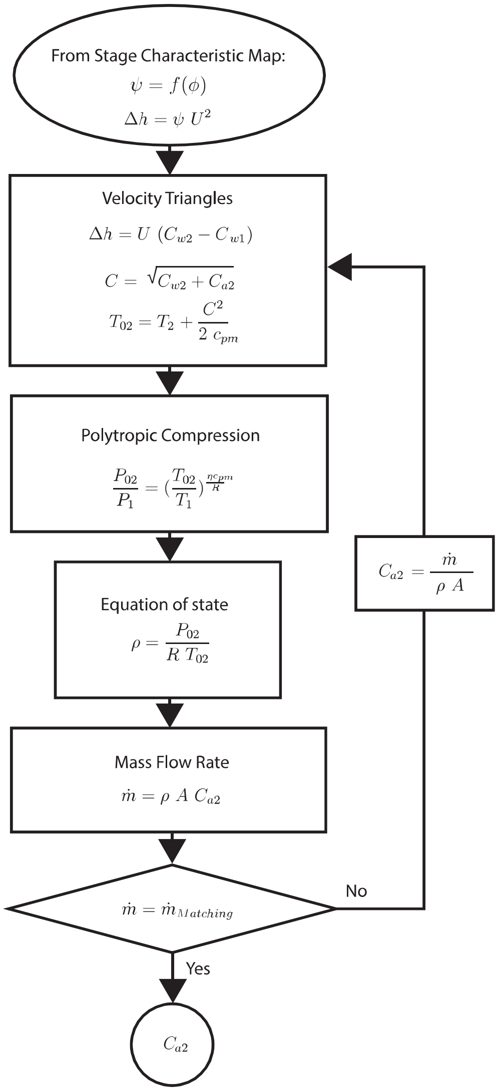

Fig. 4. Axial velocity calculation flowchart.

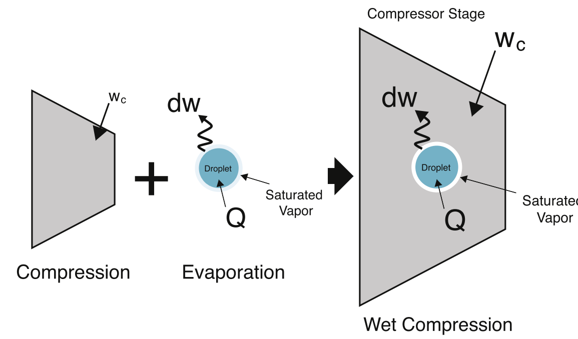

Fig. 6. Schematic of wet compression simulation.

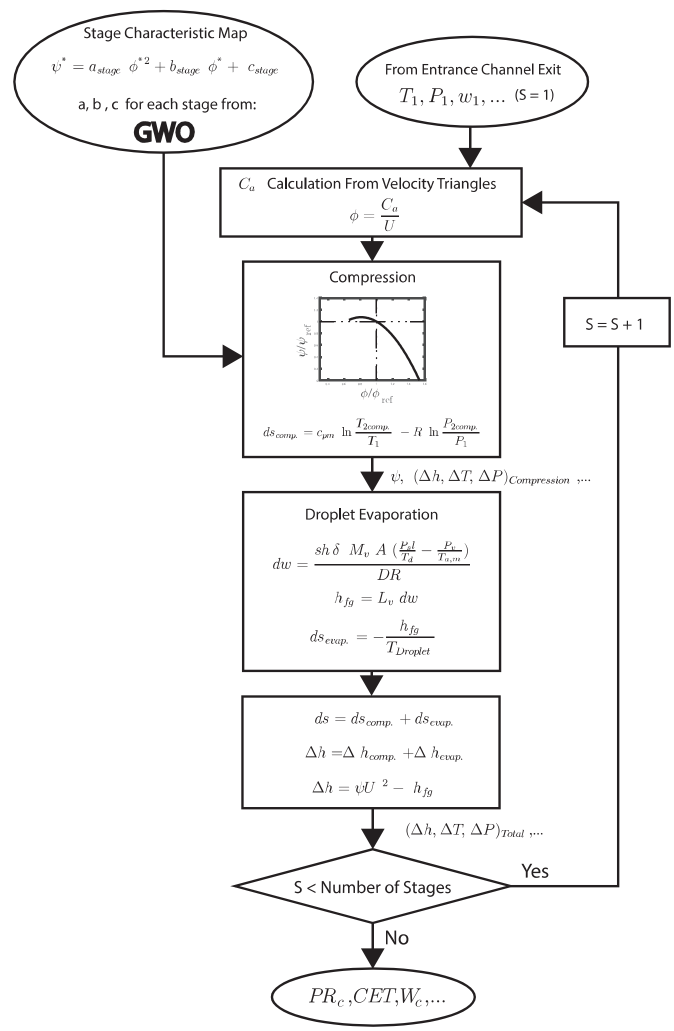

Fig. 7. Wet compression flowchart.

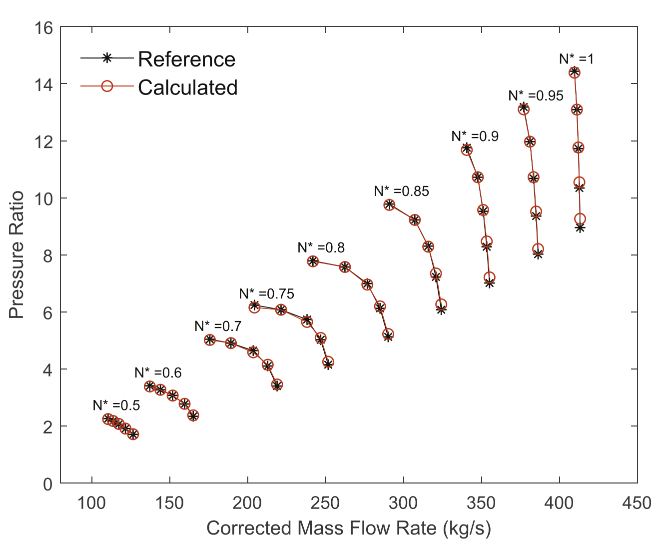

Fig. 5. Calculated and experimental data points on the scaled GE9171E gas turbine map.

(23) ΔT and ΔP for each stage can be calculated. Fig. 7 shows the wet compression flow chart and the procedure of computing the off-design compressor operating points.

4. Results and discussion

4.1. Validation study

To assess the validity of the proposed turbomachinery and thermodynamic model, results were compared with the corresponding values reported by Bhargava and Meher-Homji (2005). Calculations were performed for the GE9171E gas turbine with the design data given in Table 1 for four off-design operating conditions. Calculated and reported values for important gas turbine performance parameters are reported in Table 2, where C, R, and Δ indicate the calculated values, reported values by Bhargava and Meher-Homji (2005), and the percentage difference ($\Delta = \frac{|C-R|}{R} \times 100$), respectively. Results show that there is an excellent agreement between calculated and reported values, where the mean percentage difference of less than 3% is obtained for all the cases. In dry condition (no inlet cooling), the mean percentage difference of 1.85% indicates the accuracy of the matching and stage stacking algorithms in the prediction of the gas turbine operating point at off-design conditions. The maximum percentage difference at this operating condition is related to the fuel mass flow rate ($\dot{m}_f$), and it is equal to 7.98%. It may be due to the fact that a simple model is used for simulation of the combustion chamber, as the focus is mainly on the accurate simulation of the compressor. Implementation of fogging operation at the entrance channel leads to temperature reduction, and consequently, increase of the air density, which farther results in the increase of the compressor mass flow inlet ($\dot{m}_c$). Moreover, at a constant revolutions per minute (RPM), non-dimensional rotational speed increases with the decrease of the CIT, and eventually, the compressor operating point is matched at a point with a higher pressure ratio comparing to dry condition. The compressor power input ($\dot{W}_c$) is also increased with the increase of the $\dot{m}_c$ and compressor pressure ratio. As a result of the increase in $\dot{m}_c$, $\dot{m}_f$ is increased, and along with the higher pressure at the turbine inlet, leads to an increase in the turbine power output. In general, the fogging operation leads to higher net power output ($\dot{W}_{\text{net}}$) comparing to the dry condition. From Table 2, it can be seen that the developed algorithm is well able to predict gas turbine characteristics in fog operating condition resulting in mean percentage difference of 2.39%. Plus the effects of saturated fogging, in the wet compression process, liquid water droplets inter the compressor and reduce the work that is needed for compression. Higher mass flow and fuel rate together with higher pressure at the turbine inlet enhance the turbine power output, and in general, the net power output. The effect of the wet compression process on the compressor stages would be farther discussed in detail in Section 4.2. Here, it can be seen in Table 2 that there is a good accordance between calculated and reported data for the wet compression with oversprays of 1% and 2%, where mean percentage difference of 2.70% and 2.94% are acquired, respectively.

Besides the increase of the mass flow due to the injection of the water droplets, cooling processes leads to the increase of the dry mass flow rate, and both effects have been considered in this study. Calculated values for the inlet mass flow rate and the injected water are reported in Table 3 for the GE9171E gas turbine for four off-design operating condition corresponding to Table 2. Here, we report the total mass flow rate of the compressor, $\dot{m}_c$, rate of water injection due to the saturated fogging process, RWI_{SFo}, rate of water injection due to the overspray, RWI_{os}, and the gas air mass flow rate at the input of the entrance channel, $\dot{m}_a$. We also report the changes in mass flow rate with Δ.

It can be seen in Table 3 that the rate of water injection in the inlet fogging process is 2.152 (kg/s), and the increase in the inlet gas air mass flow rate is 15.86 (kg/s). The comparison of the increase in mass of air flow with the injected water shows that due to cooling processes, the compressor operating point is matched at a point with a higher inlet mass flow rate comparing to dry condition. In fact, only about 11.95% of the increase in the inlet mass flow rate in the fogging cooling approach is due to the injected water directly. Results showed that this value is 23.94% at 1% overspray and 32.35% at 2% overspray.

Moreover, the results of the present simulation are compared with the experimental and computational results of Utamura et al. (1999) and simulation results of Bagnoli et al. (2008) for GEF9E gas turbine. The design data of the GEF9E gas turbine are reported in Table 4. Figs. 8 and 9 depict the variation of relative change in thermal efficiency and net power output as a result of inlet fogging and overspray. Operations have been performed at the ambient condition with a temperature of 29.7° and relative humidity of 70%. Inlet fogging and overspray have been conducted using water droplets with a diameter of 10 μm. It can be seen that both thermal efficiency and net power output changes are calculated with acceptable accuracy. The change in the slope of the net power output increase is due to the arrival of the liquid water droplets to the compressor and start of the wet compression process.

4.2. Stage stacking results

In this section, the focus is on the effect of the presence and evaporation of very small liquid water droplets on the characteristic of the compressor stages. Variation of flow coefficient, load coefficient, exit temperature, the relative change in pressure, pressure ratio, droplet diameter, and polytrophic efficiency are investigated through the stages of the GE9171E compressor. Results are reported for five test cases. The dry case at $T_{\text{amb.}} = 43^{\circ}$ and RH = 40% according to the results reported in Table 2, and wet cases at saturated fogging and 1%, 2% and 3% overspray. The subscript amb. shows the values related to the ambient. The main idea in the wet compression process is to deviate the compression process from a polytropic process toward an isothermal process to reduce the work which is needed for the compression. This is performed by the evaporation of liquid water droplets inside the compressor stages and reduction of the mixture temperature due to the heat exchange with the water droplets while the compression itself increases the mixture temperature. Fig. 10 shows the variation of the stage exit temperature through the compressor. Also, Fig. 11 depicts the liquid water droplet diameters at the exit of each stage to declare the wet or dry working condition of stages. For the dry and saturated fogging test cases temperature rises through the compressor with almost the same slope; however, inlet cooling in the test case with saturated fogging reduces the CIT and the temperature through the compressor, consequently. It can be seen in Fig. 10 that the wet compression process decreases the slope of the temperature rise in the wet stages. With the increase of the overspray, and in overspray of 2% and 3%, in some stages, the slope of temperature rise is almost zero. In fact, the enthalpy change due to the water droplet evaporation ($-h_{fg}$) is about the enthalpy change due to the compression (ψU^2). For the dry stages, the slope of temperature rise is not changed considerably comparing to the dry and saturated fogging test cases.

In the test case with saturated fogging, the decrease in the gas mixture temperature and addition of the water droplets in the entrance channel leads to the increase of the mixture density and the compressor mass flow rate. In this case, it leads to the decrease of the axial velocity and flow coefficient (C_a/U) comparing to the dry test case as it can be seen in Fig. 12. In wet compression, the effect of the presence of liquid water droplets on the density, axial

Table 1
GE9171E gas turbine design point data at ISO condition (Bhargava and Meher-Homji, 2005).

RPM	PR	TIT (°C)	TET (°C)	$\dot{m}_c$ (kg/s)	$\dot{W}_{\text{net}}$ (MW)	HR (kJ/kWh)
3000	12.3	1124	541	410	124.7	10,603

Table 2
Comparison of calculated (C) and reported values (Bhargava and Meher-Homji, 2005) (R) for GE9171E gas turbine performance parameters at four off-design operating conditions.

	No Inlet Cooling			Saturated fogging			OS 1% + Saturated fogging			OS 2% + Saturated fogging		
	C	R	Δ	C	R	Δ	C	R	Δ	C	R	Δ
CIT (°C)	43	43	0	30.08	30	0.27	30.08	30	0.27	30.08	30	0.27
CET (°C)	387.98	386	0.51	370.82	371	0.04	326.7	330	1.00	299.19	293	2.11
PR_c	10.84	10.9	0.55	11.37	11.53	1.4	11.60	11.69	0.77	11.75	11.84	0.76
$\dot{m}_c$ (kg/s)	360.50	357.6	0.81	378.51	376.61	0.50	385.68	380.37	1.40	391.44	384.14	1.90
$\dot{W}_c$ (MW)	130.55	128	1.99	135.63	134.6	0.76	129.77	129	0.60	127.07	125	1.66
$\dot{m}_f$ (kg/s)	6.803	6.3	7.98	7.33	6.784	8.12	7.96	7.234	10.03	8.373	7.67	9.16
$\dot{W}_t$ (MW)	232.96	230.5	1.07	249.54	247.8	0.70	257.63	253	1.83	263.7	258	2.20
$\dot{W}_{net}$ (MW)	102.42	102.5	0.08	113.90	113.2	0.61	127.86	124	3.11	136.63	133	2.73
HR (kJ/kWh)	11940.25	11315	5.52	11576.13	11024	5.00	11190.55	10766	3.94	11015.23	10609	3.83
RWI_{SFo} (kg/s)	0	0	0	2.152	2.02	6.53	2.170	4.11	4.76	2.179	9.555	4.67
RWI_{os} (kg/s)	0	0	0	0	0	0	3.857			7.829		
Δ_{Mean} (%)			1.85			2.39			2.70			2.94

TIT = 1122°C (Note: for design data at ISO condition, see Table 1.
Fuel = natural gas, supplied at 25°C, LHV = 50,047 kJ/kg.
Site ambient conditions: 1.013 bar, 43°C, 40% RH.
All off-design data are given for the base load (100% load).

Table 3
Rate of the flow for GE9171E gas turbine at four off-design operating conditions corresponding to Table 2.

Cooling approach	$\dot{m}_c$ (kg/s)	RWI_{SFo}(kg/s)	RWI_{os}(kg/s)	$\dot{m}_a$(kg/s)	$\Delta(\dot{m}_a)$ (kg/s)	$\Delta(\dot{m}_c)$(kg/s)
No Inlet Cooling	360.50	0	0	360.50	NA	0
Saturated fogging	378.51	2.152	0	376.36	15.86	18.01
SFO + OS 1%	385.68	2.170	3.857	379.65	19.15	25.18
SFO + OS 2%	391.44	2.179	7.829	381.43	20.93	30.94

$\Delta(\cdot) = (\cdot)_{cooling} - (\cdot)_{dry}$

Table 4
GEF9E design point data at ISO conditions (Utamura et al., 1999).

RPM	PR	Compressor Adiabatic Efficiency	Number of Stages	TIT (°C)	TET (°C)	$\dot{M}_c$ (kg/s)	$\dot{W}_{net}$ (MW)
3000	12.4	89.9	17	1155	560	411	115

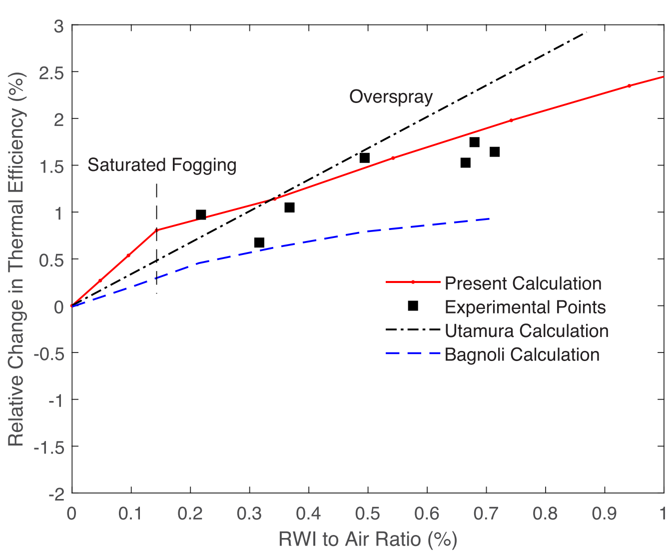

Fig. 8. Relative change in thermal efficiency versus rate of water injection; $T_{amb.}$ = 29.7°, $RH_{amb.}$ = 70% (GEF9E); comparison of the results with experimental data (Utamura et al., 1999) and numerical calculations (Utamura et al., 1999; Bagnoli et al., 2008).

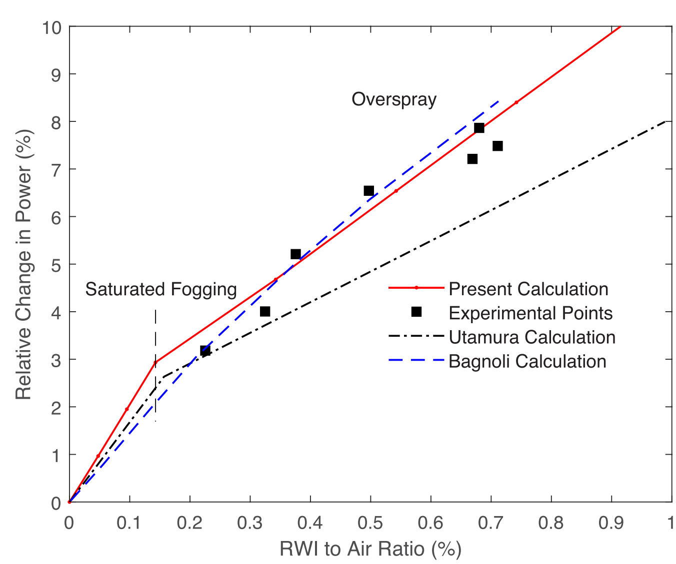

Fig. 9. Relative change in $\dot{W}_{net}$ versus rate of water injection; $T_{amb.}$ = 29.7°, $RH_{amb.}$ = 70% (GEF9E); comparison of the results with experimental data (Utamura et al., 1999) and numerical calculations (Utamura et al., 1999; Bagnoli et al., 2008).

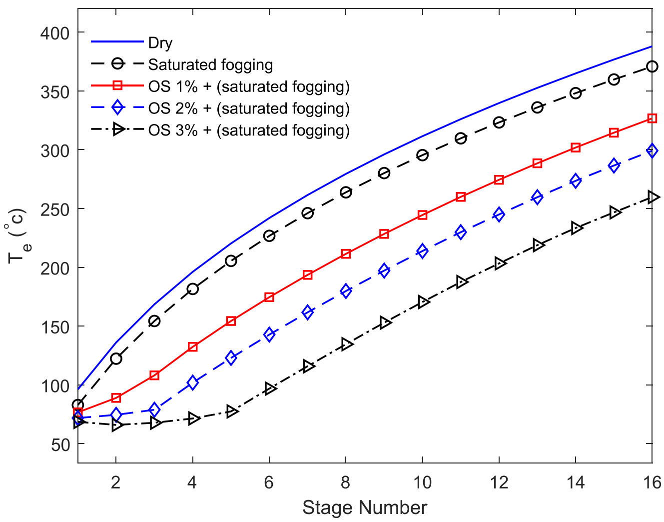

Fig. 10. Variation of exit temperature through the compressor stages; $T_{amb.} = 43^{\circ}$, $RH_{amb.} = 40\%$ (GE9171E).

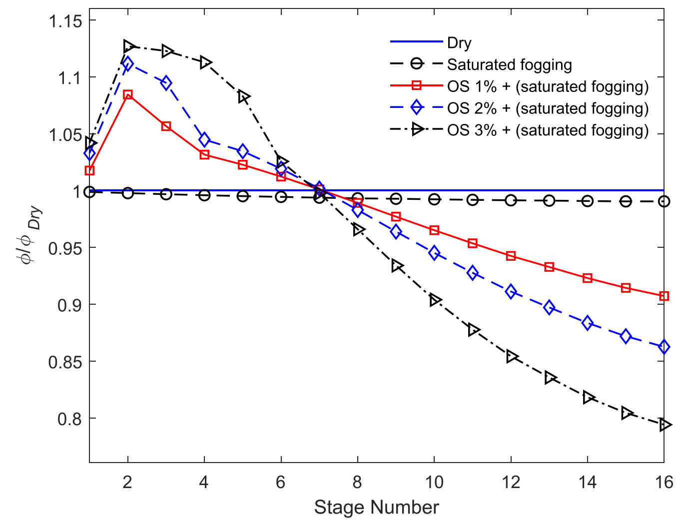

Fig. 12. Variation of flow coefficient through the compressor stages; $T_{amb.} = 43^{\circ}$, $RH_{amb.} = 40\%$ (GE9171E).

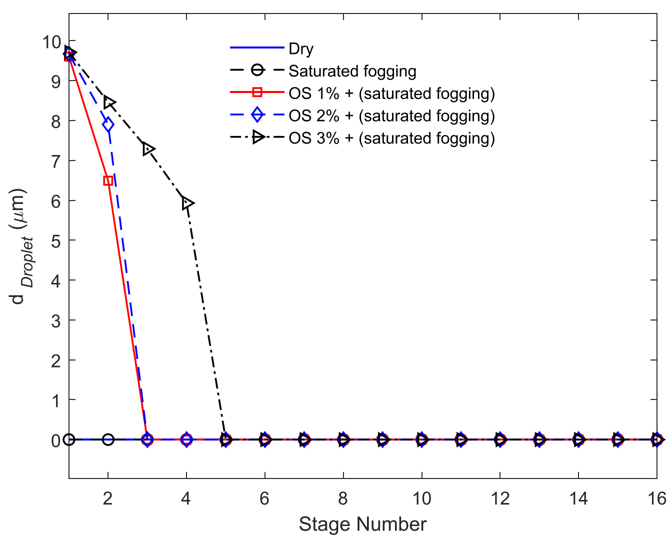

Fig. 11. Droplet diameter at the exit of compressor stages; $T_{amb.} = 43^{\circ}$, $RH_{amb.} = 40\%$ (GE9171E).

velocity, and flow coefficient is inverse. At a compressor stage, water droplet evaporation decreases both the temperature and the pressure resulting in the decrease of the density and increase of the axial velocity and flow coefficient in the wet stages (Fig. 12). Fig. 13 illustrates the variation of the relative change in the pressure through the compressor stages for various test cases. It can be seen that in the wet stages, exit pressure of the stage is decreased considerably comparing to the dry test case when overspray is applied. Decrease of the pressure is more significant according to the polytropic relation $\left(\frac{T_2}{T_1}\right)^{\frac{k}{k-1}} = \left(\frac{P_2}{P_1}\right)$, where k is the polytropic index of the wet compression process. It also can be seen in Fig. 14 where the variations of the pressure ratio are depicted through the compressor stages. In wet stages, the pressure ratio is decreased with the increase of the overspray percentage while the increase in mass flow rate results in a higher pressure ratio in dry stages. The decrease in the temperature compared to the dry test case results in a more severe decrease in pressure (Fig. 13) and decrease of the density of the moisture, and it is farther results in the velocity and mass flow increase (Fig. 12) in wet stages. However, with complete evaporation of the liquid water droplets and in the dry stages, density is increased, and the axial velocity and flow coefficient are reduced analogous to the trend that has been seen in the saturated fogging test case.

For the test case with saturated fogging, the decrease in the flow coefficient through the compressor stages results to the increase of the load coefficient as it can be seen in Fig. 15. For test cases with overspray, it is notable that in the wet stages, the load coefficient is reduced compared to the dry test case as the flow coefficient is increased. This decrease is more intense for the test cases with a higher percentage of overspray. However, at the dry stages, the load coefficient is higher than the one obtaining in the dry test case. In fact, in the wet compression process, early stages of the compressor are offloaded where the later ones are overloaded comparing to dry operating condition, and it may enhance the risk of the surge in last stages (see Fig. 16).

As it is mentioned in Section 3, the generalized curve (Eq. (18)) proposed by Howell and Bonham (1950) is used for calculation of the polytropic efficiency, which represent polytrophic efficiency as a function of load and flow coefficients $\eta_p = f(\psi/\varphi)$. In wet stages, the load coefficient is decreased, and the flow coefficient is increased, so ψ/φ is reduced, which leads to an intense reduction of the polytropic efficiency. During the dry stages in the later part of the compressor, the flow coefficient is reduced, and the load coefficient is increased compared to the dry test case. Therefore, ψ/φ is increased, which farther results in a mild decrease in the polytropic efficiency comparing to the dry test case. These results indicate that the polytropic efficiency varies significantly in the wet compression process, and it cannot be considered constant.

4.3. Effect of saturated fogging and wet compression on gas turbine characteristics

The effect of wet compression process and saturated fogging on the compressor power input, compressor pressure ratio, turbine power output, gas turbine net power output, heat rate, and thermal efficiency are studied, and results are presented in Figs. 17 to 22. Results are reported for four ambient temperature 23°, 33°, 43°, and 53° at five off-design operating condition form dry to wet compression with 3% overspray and saturated fogging. Fig. 17

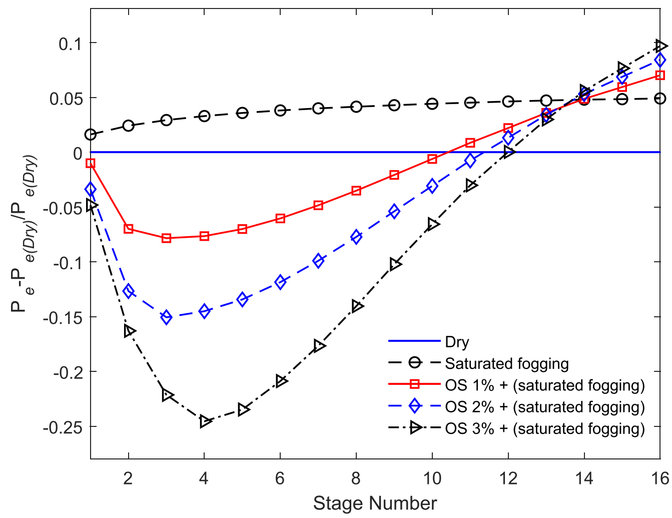

Fig. 13. Variation of relative change in pressure through the compressor stages; $T_{amb.} = 43^{\circ}$, $RH_{amb.} = 40\%$ (GE9171E).

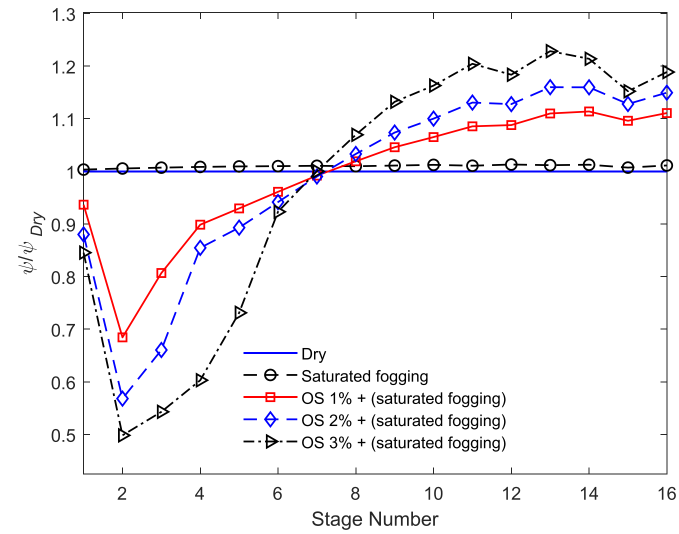

Fig. 15. Variation of load coefficient through the compressor stages; $T_{amb.} = 43^{\circ}$, $RH_{amb.} = 40\%$ (GE9171E).

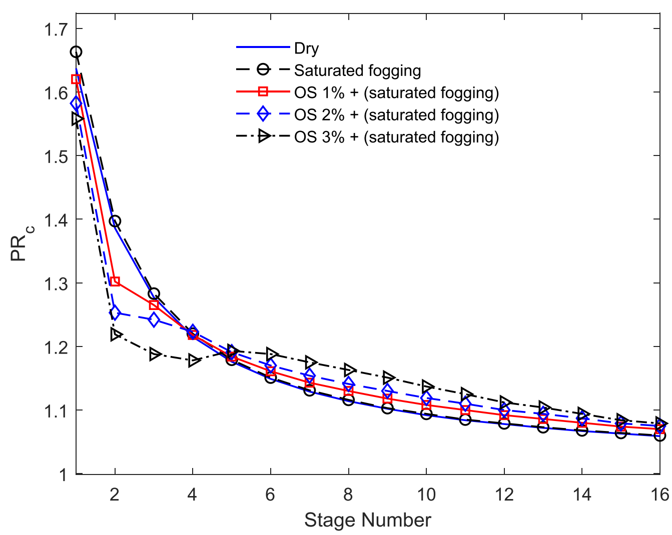

Fig. 14. Variation of stage pressure ratio; $T_{amb.} = 43^{\circ}$, $RH_{amb.} = 40\%$ (GE9171E).

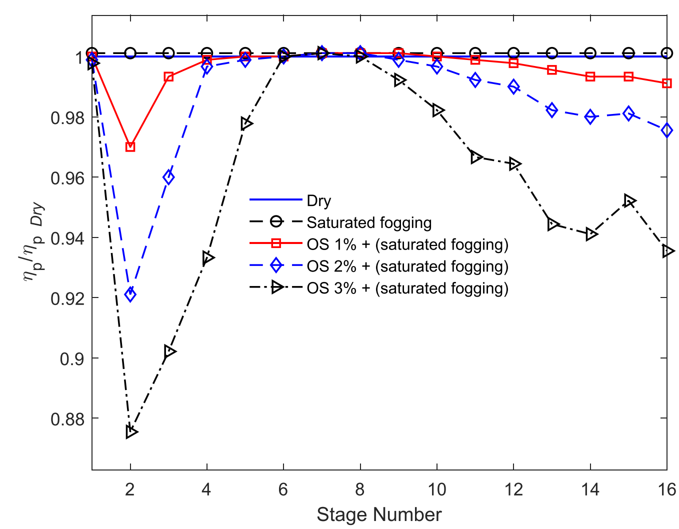

Fig. 16. Variation of polytrophic efficiency through the compressor stages; $T_{amb.} = 43^{\circ}$, $RH_{amb.} = 40\%$ (GE9171E).

depicts variation of compressor work input versus rate of water injection. With the implementation of saturated fogging for inlet cooling, it can be seen that the compressor work input is increased compared to the dry test case. For ambient temperatures of 23°, 33°, 43°, and 53° this increase is equal to 2.66%, 3.20%, 3.60%, and 4.41%, respectively, which is increased with the increase of the ambient temperature. In contrast, the compressor power input is decreased due to the wet compression process. As a result of the increase of the water injection rate, compressor work input is farther decreased because more stages work in the wet condition.

Due to the saturated fogging and overspray, both mass flow rate and pressure ratio of the compressor are increased as it can be seen in Fig. 18 for the compressor pressure ratio. The increase in the mass flow rate results in an increase in fuel rate. Moreover, the pressure at the turbine inlet is increased due to the increase of the compressor pressure ratio. Consequently, a higher mass flow rate with higher pressure results in an increase in turbine work output as it can be seen in Fig. 19. The slope of the changes in turbine work output is steeper from dry to saturated fogging comparing to the changes from saturated fogging to the cases with overspray for all the ambient temperatures. However, the decrease of the compressor input power in wet compression process compensates the moderate increase of the turbine work output, and it can be seen in Fig. 20 that the net power output increases with almost a same slope in saturated fogging and wet compression for the mentioned gas turbine. It is also notable that compressor work input, turbine work output, and net power output are all decreased in every operating condition with the increase of the ambient temperature.

The quantity of overspray for each engine is the concern of wet compression technique. One of the limitations of this approach is whole water should evaporate inside the compressor. The presence of liquid water led to reduction of pressure ratio (Fig. 18), and with high amounts of water injection compressor may not be able to recover the pressure. In addition, in some cases, although all the water droplets evaporate inside the compressor, due to the high reduction of CET and fixed TIT, the efficiency gain will reduce. The achieved efficiency depends on fuel rate consumption. By considering fixed TIT, the lower temperature at the compressor exit due to

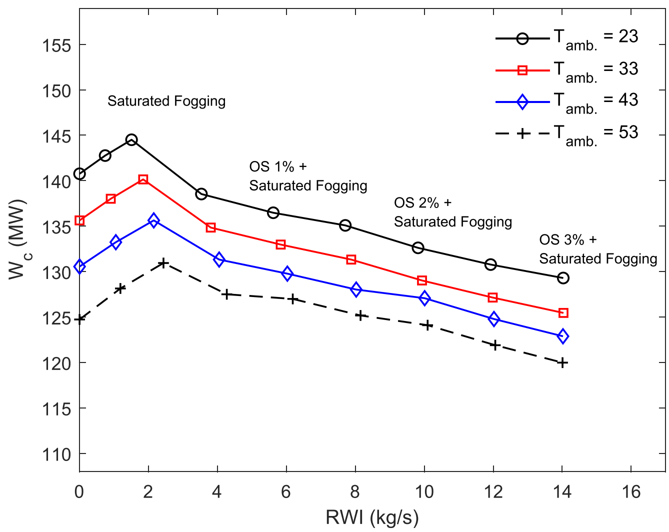

Fig. 17. Compressor power input variation versus rate of water injection at working conditions with various $T_{amb.}$ (GE9171E).

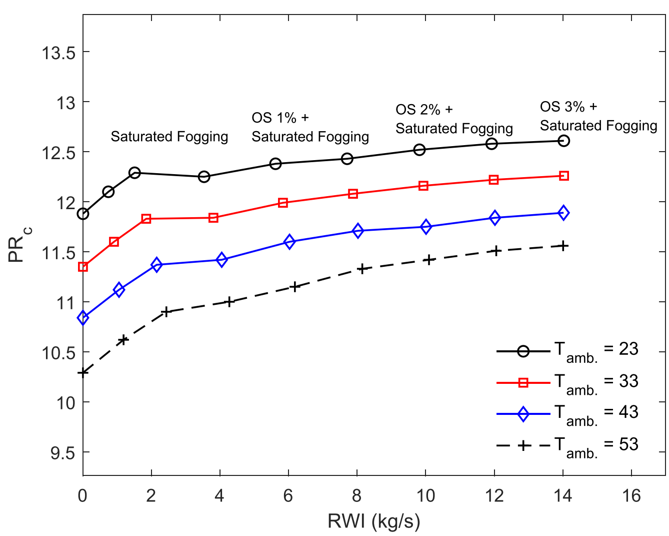

Fig. 18. Compressor pressure ratio variation versus rate of water injection at working conditions with various $T_{amb.}$ (GE9171E).

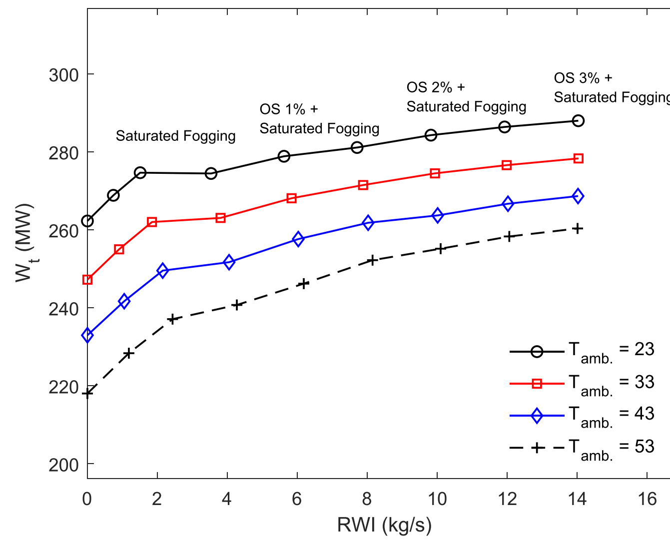

Fig. 19. Turbine power output variation versus rate of water injection at working conditions with various $T_{amb.}$ (GE9171E).

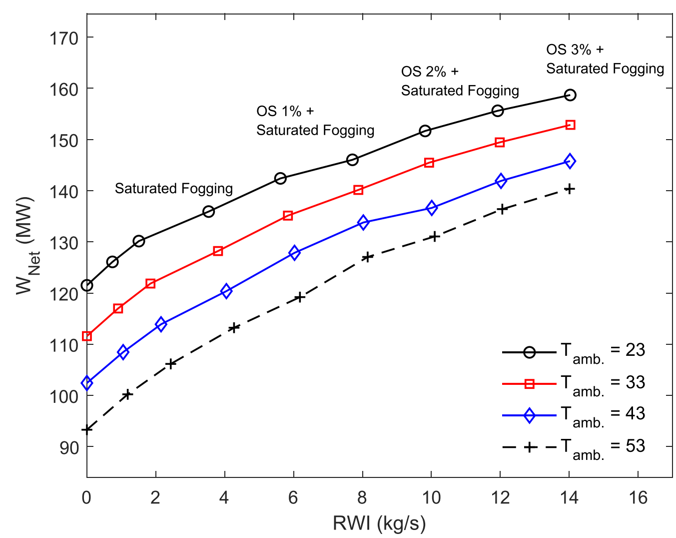

Fig. 20. Net power output variation versus rate of water injection at working conditions with various $T_{amb.}$ (GE9171E).

the overspray process will result in higher fuel rate, which has an inverse effect on efficiency. However, the turbine output power will increase (Figs. 20 and 22). The variation of heat rate and thermal efficiency of the gas turbine due to the inlet cooling and wet compression are illustrated in Figs. 21 and 22, respectively. With the implementation of inlet cooling toward the saturated fogging, it can be seen that the heat rate is reduced. This decrease occurs with a sharper slope for working condition with higher ambient temperatures. With a higher rate of water injection and overspray, heat rate is decreased until a specific amount of water injection is reached for each ambient temperature, and after that, with the increase of the water injection, the heat rate is increased. It is shown that the net power output of the gas turbine is increased monotonically with the increase of water injection rate, which is the reason of the heat rate reduction with the increase of the water injection rate. However, a high amount of water injection leads to a reduction of the CET, and in a cycle with constant TIT, results in an increase in fuel mass flow rate. Increase of the compressor mass flow rate due to the overspray and inlet cooling is another reason for the fuel flow rate increase. As a result of the fuel flow rate increase, the heat rate is increased from its minimum. Moreover, the thermal efficiency of the gas turbine is decreased with the increase of the heat rate (Fig. 22). The results show that although an increase of overspray percentage leads to a monotonic increase of the net power output, it does not result in an advancement in thermal efficiency at every amount of water injection rate. Maximum thermal efficiency is gained at a specific percentage of overspray, and it changes with the change of the ambient condition. Fig. 23 depicts the amount of overspray percentage in which the thermal efficiency is maximum versus the ambient temperature. In the working condition with higher ambient temperatures, the maximum of the thermal efficiency occurs when a higher percentage of overspray is implemented. It means that it is feasible to use higher water injection rates in higher ambient temperatures without the probability of thermal efficiency reduction. In Fig. 23 the increase of the overspray percentage in the blue zone will lead to the

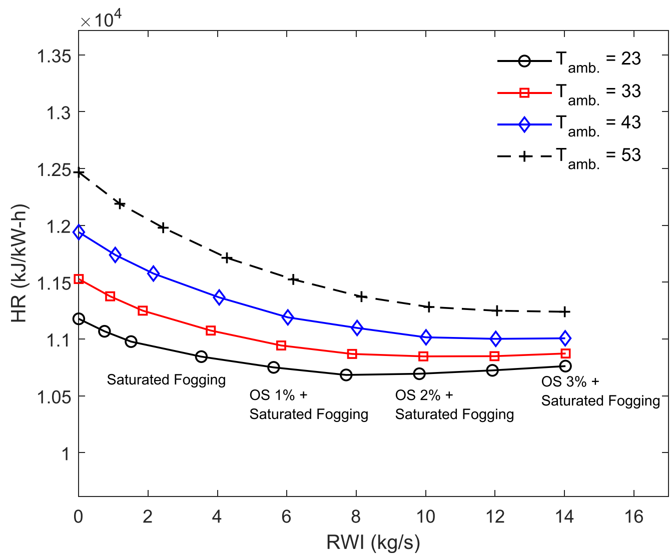

Fig. 21. Heat Rate variation versus rate of water injection at working conditions with various $T_{amb.}$ (GE9171E).

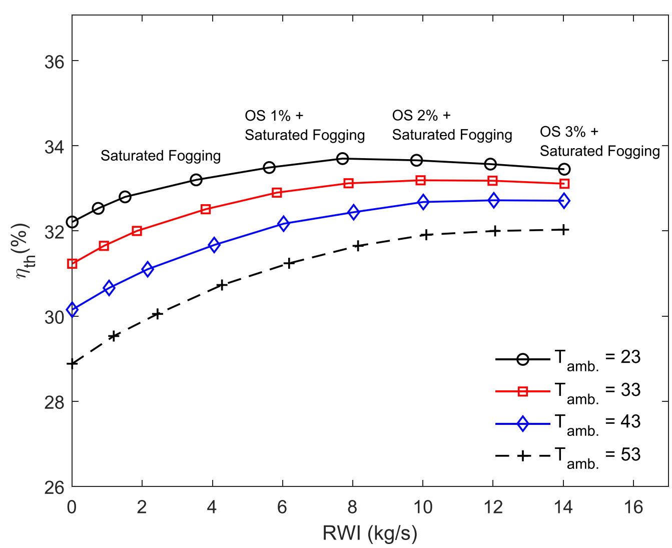

Fig. 22. Thermal efficiency variation versus rate of water injection at working conditions with various $T_{amb.}$ (GE9171E).

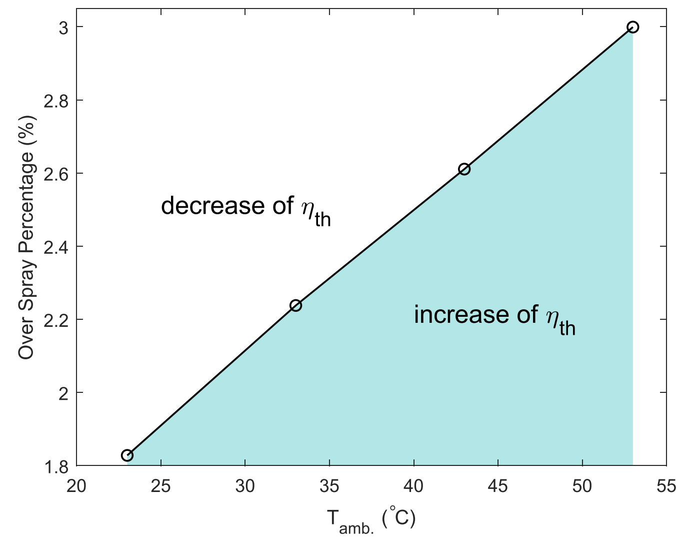

Fig. 23. Overspray percentage corresponding with maximum thermal efficiency gain as the result of wet compression and saturated fogging (GE9171E).

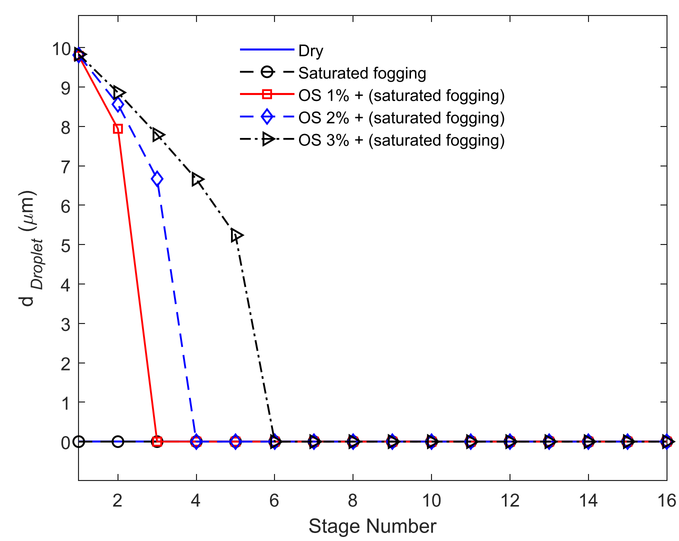

Fig. 24. Droplet diameter at the exit of compressor stages; $T_{amb.} = 23^{\circ}$, $RH_{amb.} = 40\%$ (GE9171E).

advancement of the thermal efficiency while on the other hand, it results to the decrease of the thermal efficiency. Table 5 represent the variation of CET, mass fuel rate, net power output, and thermal efficiency with the amount of water injection at the ambient with the temperature and relative humidity of 23° and 40%, respectively. It can be seen that increase of the overspray percentage from 1.5% to 3% leads to reduction of thermal efficiency from 33.7% to 33.45% while it results in an increase of net power output from 146.03 to 158.69 MW (see Fig. 24).

The data in Table 6 shows the results of thermal efficiency and total net power output corresponding to the Figs. 20 and 22 in varying water injection rate and ambient temperature with relative humidity of 40%.

It can be seen that increase of the overspray percentage from dry condition to 2% overspray leads to increase in thermal efficiency from 32.21% to 33.66% at the ambient with temperature and relative humidity of 23° and 40%, respectively. The relative increase in the thermal efficiency at the 23°, 33°, 43°, and 53° are 4.5%, 6.28%, 8.39%, and 10.49%, respectively. Implementation of the wet compression system leads to an increase in the thermal efficiency from 30.15% (at 43°) to 32.68%. Using this method the thermal efficiency is improved by 2.53% (8.39% relative change) at this ambient temperature. The simulation results prove that the wet compression is a very efficient technique to improve power output and efficiency when ambient temperature increases.

4.4. Effect of ambient relative humidity and temperature

To study the effect of ambient temperature on the compressor stages at the fogging and wet compression working conditions, results of compressor modeling are compared for two ambient temperatures of 23° and 43°. Fig. 25 presents relative change in exit pressure of each compressor stage for the mentioned ambient temperatures. Results are presented for saturated fogging, and overspray of 1% and 3%. Open markers correspond with $T_{amb.} =$

Table 5
GE9171E Gas turbine performance parameters for different working conditions at the ambient with $T_{amb.} = 23^{\circ}$ and $RH_{amb.} = 40\%$.

	D	SFo	SFo +0.5% OS	SFo +1% OS	SFo +1.5% OS	SFo +2% OS	SFo +2.5% OS	-SFo + 3% OS
CET ($^{\circ}C$)	367.25	356.02	331.42	311.48	300.13	276.86	258.76	243.37
$\dot{M}_f$ (kg/s)	7.556	7.948	8.2	8.516	8.679	9.024	9.283	9.5
$\dot{W}_{net}$ (MW)	121.51	130.15	135.92	142.4	146.03	151.67	155.61	158.69
η_{th} (%)	32.21	32.8	33.2	33.49	33.7	33.66	33.57	33.45

Table 6
Thermal efficiency and total net power of the GE9171E gas turbine corresponding to the data of the Figs. 20 and 22 in varying water injection rate and ambient temperature with relative humidity of 40%.

Outputs	$T_{amb.}$	D	SFo	SFo + OS 1%	SFo + OS 2%	$\Delta_{SFo+OS\ 1\%}$	$\Delta_{SFo+OS\ 2\%}$
η_{th} (%)	23	32.21	32.8	33.49	33.66	3.97%	4.50%
	33	31.23	32.01	32.90	33.19	5.35%	6.28%
	43	30.15	31.10	32.17	32.68	6.70%	8.39%
	53	28.88	30.05	31.24	31.91	8.17%	10.49%
$\dot{W}_{net}$ (MW)	23	121.51	130.15	142.4	151.67	17.19%	24.82%
	33	111.59	121.86	135.13	145.47	21.10%	30.36%
	43	102.42	113.90	127.86	136.63	24.84%	33.40%
	53	93.30	106.16	119.21	131.06	27.77%	40.47%

$\Delta(\cdot) = \frac{(\cdot)_{cooling} - (\cdot)_D}{(\cdot)_D} \times 100$

23°, and close markers are related to the values for $T_{amb.} = 43^{\circ}$. Liquid water droplet diameter at the exit of each stage is also depicted in Figs. 11 and 25 for the ambient temperature of 43° and 23°, respectively. It can be seen in Fig. 25 that the pressure change relative to stage exit pressure at dry condition is bigger for the test case with the higher ambient temperature for all three working conditions of saturated fogging, and overspray of 1% and 3%. It indicates that at higher ambient temperatures, the fogging and wet compression processes are more effective.

Also, the effect of ambient temperature and relative humidity on the performance of the inlet fogging and wet compression processes is investigated. Relative humidity of the ambient is varied from 10% to 100% for the range of ambient temperature from 5° to 65°. Results of gas turbine simulation are reported for three working conditions of dry, saturated fogging, and wet compression with an overspray of 1%. To have a proper insight on the performance of the gas turbine, results are presented as operating points on the compressor overall characteristic map. At first, relative humidity is changed from 10% to 100% for three ambient temperatures of 5°, 25°, and 45°, and the corresponding results are depicted in Fig. 26. It can be concluded that the effect of relative humidity is more significant in higher ambient temperatures. Moreover, it can be seen that with the implementation of the inlet fogging and overspray, the effect of the relative humidity is extended in the same direction. In higher ambient temperatures with lower relative humidity, fogging and wet compression processes are more effective, and the operating points in these conditions more deviate from the one in dry condition. Fig. 27 presents the variation of operating point in three constant relative humidity of 10%, 40%, and 80% as a result of ambient temperature change from 5° to 65°. With the increase of the ambient relative humidity, the effect of saturated fogging is diminished where the operating points related to

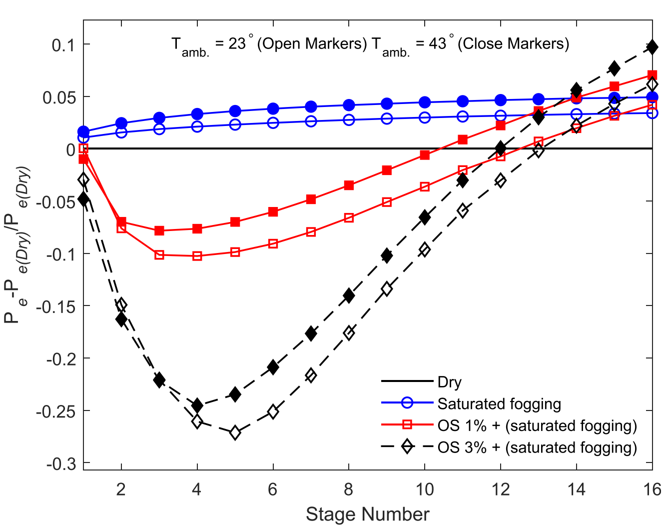

Fig. 25. Comparison of variation of relative change in pressure through the compressor stages for $T_{amb.} = 43^{\circ}$ and 23°, $RH_{amb.} = 40\%$ (GE9171E).

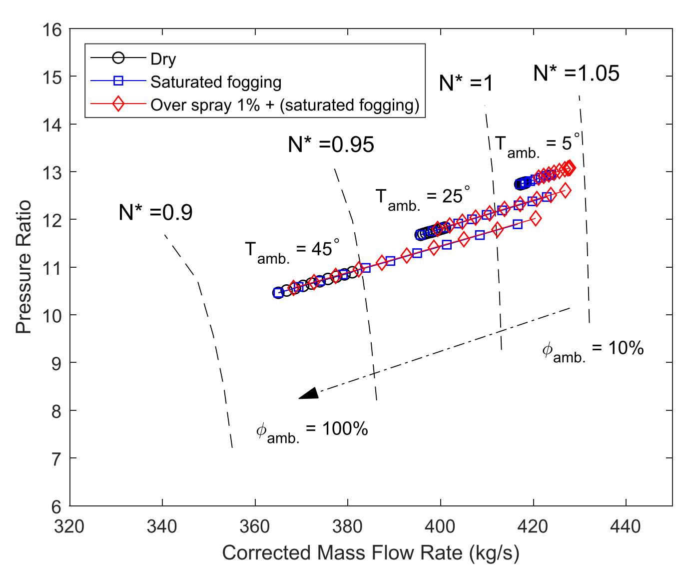

Fig. 26. Variation of compressor operating point for three working condition of dry, saturated fogging, and saturated fogging with overspray of 1%; the effect of $RH_{amb.}$ change at three $T_{amb.}$ of 5°, 25°, and $45^{\circ}C$ (GE9171E).

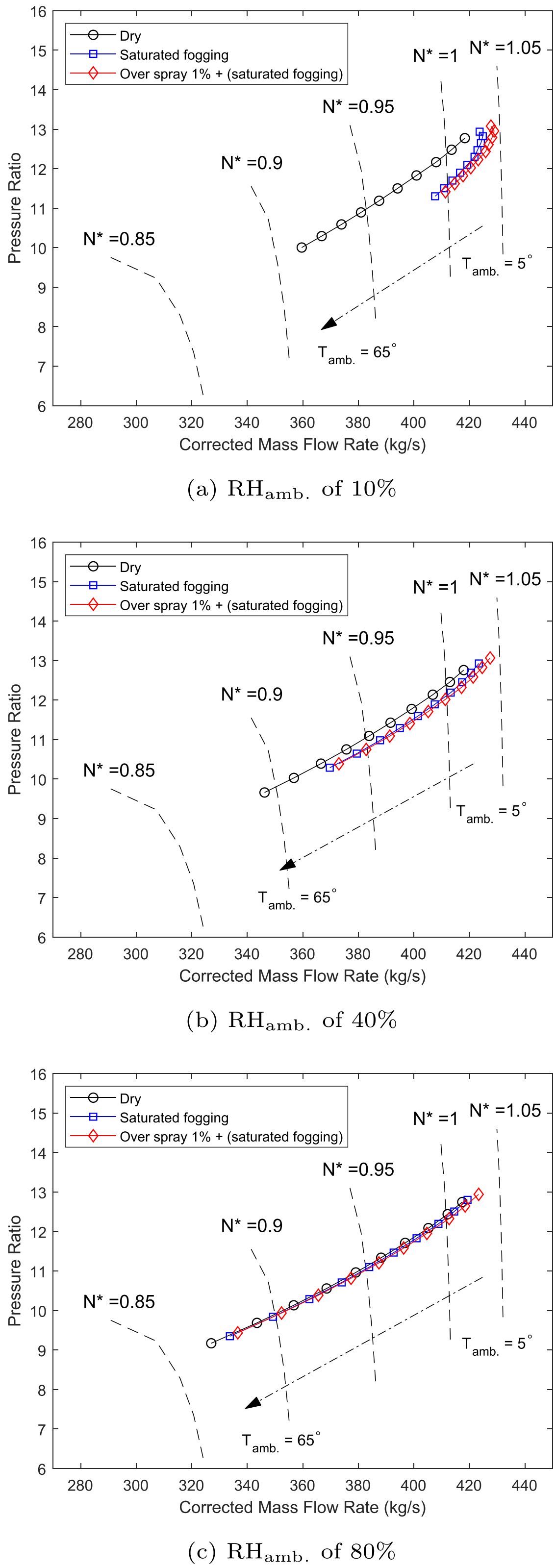

Fig. 27. Variation of compressor operating point for three working condition of dry, saturated fogging, and saturated fogging with overspray of 1%; the effect of $T_{amb.}$ change at three different ambient relative humidity of (a) 10%, (b) 40%, and (c) 80% (GE9171E).

the saturated fogging condition move towards the dry operating points. However, the deviation of operating points related to the overspray of 1% from the saturated fogging operating points remains unchanged with the variation of the ambient relative humidity. It can be seen that at lower relative humidities the wet running line more deviates from the dry running line. The gain in thermal efficiency and net power output due to the wet compression with an overspray of 1% in various ambient temperatures and relative humidities is also investigated, and results are depicted in Fig. 28. In this figure, the size of the circles indicates the ambient temperature, and the color variation corresponds with the relative humidity variation. Both thermal efficiency and net power output are normalized with their values at the dry condition. It can be seen that the highest thermal efficiency and net power output gain are acquired from wet compression at the ambient condition with the highest temperature and lowest relative humidity.

Five different locations are chosen in order to evaluate the performance of the wet compression evaporative cooling technique in different climatic conditions: Abadan (Iran), Cairo (Egypt), Darwin (Australia), Marseille (France), and Guangzhou (China). Climatic data are collected from WeatherAtlas (2002–2020). The most important parameters for industrial stationary gas turbine users are the variation of net output power and thermal efficiency. In order to provide more practical data, quantitative results are presented for these two important parameters for these five cities. The results for evaporative cooling with saturated fogging plus 1% overspray are shown in Table 7 where the critical ambient temperature and relative humidity are presented for the five cities.

5. Sensitivity analysis with variable importance

In this section, a sensitivity analysis of the wet compression process is performed with the use of a newly developed technique based on variable importance (VI). Through the sensitivity analysis, it is of interest to determine how different values of independent variables at the input affect a particular variable at the output. The sensitivity of an input variable is an indication for the impact that variation of that input could have on the output; the greater sensitivity of input, the greater variation of the output and vice versa. Here, the sensitivity of five independent variables, namely,

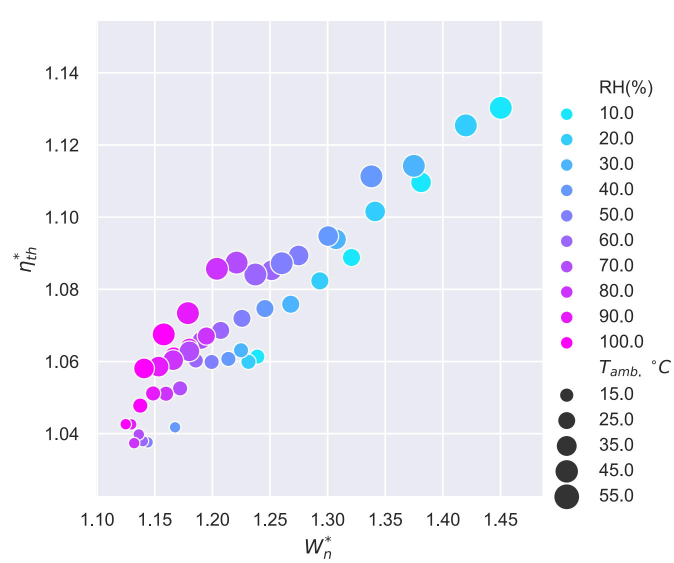

Fig. 28. Variation of net power output and thermal efficiency gain due to the wet compression with overspray of 1% and saturated fogging; 15 ⩽ T⩽amb. 55 and 10 ⩽ $RH_{amb.}$%⩽ 100 (GE9171E).

Table 7
Operating parameters of the GE9171E gas turbine for five different ambient air condition under saturated fogging and overspray of 1%.

City	Ambient air condition	$\dot{W}_{\text{net}}$ (MW)	η_{th} (%)	$\dot{W}_{net,D}$ (MW)	$\eta_{th,D}$ (%)	$\lvert\dot{W}_{\text{net}}\rvert$ (MW)	$\Delta\dot{W}_{\text{net}}$ (%)	$\lvert\eta_{th}\rvert$ (%)	$\Delta\eta_{th}$ (%)
Abadan	$T_{\text{amb.}} = 45.4^{\circ}$ RH = 15%	134.07	32.80	100.73	30.27	33.34	33.10	2.53	8.36
Cairo	$T_{\text{amb.}} = 34.7^{\circ}$ RH = 58%	130.28	32.43	109.79	30.89	20.49	18.66	1.54	4.99
Darwin	$T_{\text{amb.}} = 31.4^{\circ}$ RH = 40%	136.33	33.00	113.13	31.39	23.20	20.51	1.61	5.13
Guangzhou	$T_{\text{amb.}} = 32.8^{\circ}$ RH = 82%	125.02	32.11	111.38	30.90	13.64	12.25	1.21	3.92
Marseille	$T_{\text{amb.}} = 29.1^{\circ}$ RH = 52%	135.86	32.96	115.28	31.54	20.58	17.85	1.42	4.50

$\Delta(\cdot) = \frac{(\cdot)_{cooling} - (\cdot)_D}{(\cdot)_D} \times 100, |(\cdot)| = (\cdot)_{cooling} - (\cdot)_D.$

design compressor pressure ratio, ambient temperature, ambient relative humidity, non-dimensional rotating speed, and non-dimensional TIT, is examined. The effects of variations of the input parameters on the ten output parameters are assessed and reported. A newly developed method in the domain of machine learning is used for this peruse. To this end, the importance of a feature is measured by calculating the increase in the model's prediction error after permuting the feature, and it is called *feature importance*. A feature is important if shuffling its values increases the model error because in this case, the model relied on the feature for the prediction. A feature is unimportant if shuffling its values leaves the model error unchanged because in this case, the model ignored the feature for the prediction. The permutation feature importance measurement was introduced by Breiman (2001) for random forests. Based on this idea, Fisher et al. (2018) proposed a model-agnostic version of the feature importance and called it model reliance. Here, we implement the method of Fisher et al. (2018) to perform a variable importance analysis on the input parameters of the wet compression process.

To this end, an artificial network network (ANN) was applied to find correlation patterns among the data set. ANNs are universal approximators that have been widely used for engineering applications (Eivazi et al., 2020; Shin et al., 2019; Khoshroo et al., 2018). Based on the developed gas turbine simulation code the data was produced for different gas turbines with various design data in different climate conditions. In order to investigate the sensitivity analysis of gas turbine input data on operating parameters a multilayer perceptron (MLP) network is used to model the system. MLPs are the most basic type of ANNs and consist of three or more layers of nodes. The workhorse of learning with ANN are the feedforward and backpropagation algorithms, which computes the parameters in each node from the training data. Let X be an input and Y be an output; the objective is to learn the mapping $f: X \rightarrow Y$ from the training set such that a loss function $L(f(x); y)$ is minimized. In an MLP network, the mapping $f(x)$ can be decomposed to a sequence of linear matrix transformation followed by an element-wise nonlinear function called activation function (e.g., tanh). Fig. 29 summarizes the basic structure of an MLP. The evaluation of $Y = f(X)$ is conducted using Eq. (24):

$$Y_i = g_i(\mathbf{W}_i \times Y_{i-1} + b_i), g(x) = tanh(x), \tag{24}$$

where for layer i, g_i are the activation functions, $\mathbf{W}_i$ are the weight matrices, and b_i are the biases, which perform together a transformation from one hidden layer to the next. The goal of training an MLP is to determine $\mathbf{W}_i$ and b_i using training data, for the given activation functions. The weights and biases are updated using the back-propagation algorithm, which involves the use of gradient descent. For the training runs in this work, the adaptive moment estimation (Adam) optimizer (Kingma and Ba, 2015) is used. Adam has an adaptive learning rate method which is commonly used to train deep networks. The mean-squared error (MSE) is used as the loss function as a standard choice for regression problems. We also use the coefficient of determination, R^2, to assess the performance of the trained networks:

$$MSE = \frac{\sum_{i=1}^{m}(y_i - \hat{y}_i)^2}{n}, \tag{25}$$

$$R^2 = 1 - \frac{\sum_{i=1}^{m}(y_i - \hat{y}_i)^2}{\sum_{i=1}^{m}(y_i - \bar{y})^2}, \tag{26}$$

where, y_i is the real data, $\hat{y}_i$ represents the predicted data, and $\bar{y}$ is the mean of the real data. In addition, m is the number of samples. Here, Input and output layers contain 5 and 10 neurons, respectively, which are the inputs and outputs of the gas turbine analysis algorithm. The output parameters are non-dimensional relative to the corresponding values in dry condition (indicated by *) to asses the impact of the input parameters on the performance of the wet compression process. The data set was randomly split into two sets, 80% for model training (to compute the gradient and updating of the network parameters, i.e. weights and biases—the training set) and 20% for model testing (10% of the data is split for the validation, and 10% is specified for the test). The model weights were randomly initialized and the training process was stopped when the network began to overfit the data. For developing a proper ANN, the number of layers, the number of neurons in the hidden layers, the learning rate, the activation functions in the hidden layers, and the number of epochs for model training should be considered. A trial-and-error procedure was applied to determine the best set of these hyperparameters. Results are reported in Table 8.

Based on the results, we choose an architecture containing three

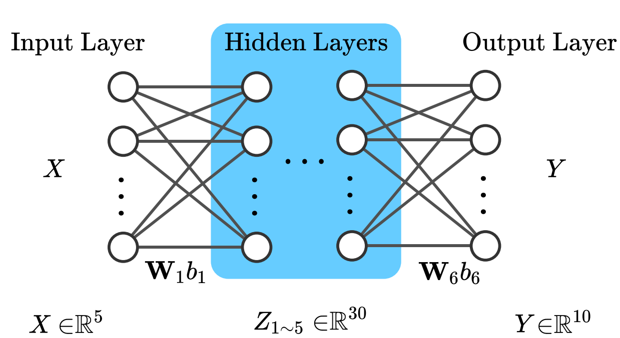

Fig. 29. Neural network architecture.

Table 8
Results of the hyperparameter analysis of the MLP neural network. The best-performing model is shown in boldface.

Model	Number of hidden layers	Number of neurons	Activation function	Optimizer	Validation loss
MLP1	5	50	tanh	Adam	7.02×10^{-4}
MLP2	5	50	sigmoid	Adam	7.04×10^{-4}
MLP3	5	50	relu	Adam	1.03×10^{-3}
MLP4	**5**	**30**	**tanh**	**Adam**	$\mathbf{6.66} \times 10^{-4}$
MLP5	5	30	sigmoid	Adam	1.04×10^{-3}
MLP6	5	30	softplus	Adam	1.23×10^{-3}
MLP7	5	30	relu	Adam	2.49×10^{-3}
MLP8	5	10	tanh	Adam	5.51×10^{-3}
MLP9	5	10	sigmoid	Adam	2.27×10^{-3}
MLP10	3	50	tanh	Adam	7.49×10^{-4}
MLP11	3	50	sigmoid	Adam	9.63×10^{-4}
MLP12	3	50	softplus	Adam	1.88×10^{-3}
MLP13	3	50	relu	Adam	3.17×10^{-3}
MLP14	3	30	tanh	Adam	8.13×10^{-4}
MLP15	3	30	sigmoid	Adam	1.01×10^{-3}
MLP16	3	30	softplus	Adam	1.65×10^{-3}
MLP17	3	30	relu	Adam	3.12×10^{-3}
MLP18	3	10	tanh	Adam	9.56×10^{-3}
MLP19	3	10	sigmoid	Adam	1.79×10^{-3}
MLP20	3	10	softplus	Adam	2.79×10^{-3}
MLP21	3	10	relu	Adam	6.41×10^{-3}
MLP22	1	50	tanh	Adam	1.62×10^{-3}
MLP23	1	50	sigmoid	Adam	1.14×10^{-3}
MLP24	1	30	tanh	Adam	2.24×10^{-3}
MLP25	1	30	sigmoid	Adam	1.19×10^{-3}
MLP26	1	10	tanh	Adam	1.01×10^{-2}
MLP27	1	10	sigmoid	Adam	1.16×10^{-2}
MLP28	5	30	tanh	SGD	1.23×10^{-2}
MLP29	5	30	tanh	Adadelta	1.38×10^{-2}

hidden layers with 50 neurons at the hidden layers (Fig. 29) as the MLP architecture. Input and output layers are linear and tanh activation function is used for hidden layers. We also tested the effect of learning rate, where the learning rate of 10^{-4} provides acceptable convergency. We tested the performance of the three optimization algorithm to update the network parameters (wights and biases), i.e., Adam (Kingma and Ba, 2015), Adadelta (Zeiler, 2012), and stochastic gradient descent (SGD), and Adam algorithm outperforms the others (Table 8). It also should be noted that to avoid overfitting the training process is stopped where more training epochs does not lead to farther reduction of the validation loss. For all the trainings the batch size is equal to 32.

Variation of two metrics of R^2 and MSE are depicted through the training procedure for the train and validation data in Fig. 30. It can be seen that the model is well fitted to the data where R^2 and MSE of 0.9889 and 6.66×10^{-4} are obtained in the prediction of the validation data. And finally, variable importance analysis is conducted on the whole data set, and results are depicted in Fig. 31. For CIT (Fig. 31a), as it is expected, it can be seen that ambient temperature and ambient relative humidity are the only two influential input parameters. It indicates that the implemented method is well capable of representing the impact of input parameters on the outputs. For CET (Fig. 31b), the influence of compressor pressure ratio is significant as well as ambient relative humidity. The effect of input parameters on the compressor mass flow rate and compressor pressure ratio are mostly influenced by the ambient temperature and ambient relative humidity analogous to the compressor power input, TET, and net power output of the gas turbine as it is shown in Fig. 31c to g. However, for turbine power output, heat rate, and thermal efficiency the influence of changes in TIT is more significant (Fig. 31h to j). It can be concluded that the influence of ambient relative humidity and ambient temperature on the performance of wet compression process are dominant with the consideration of the changes in net power output. However, with consideration of thermal efficiency, TIT is the most influential parameter on the performance of the wet compression process.

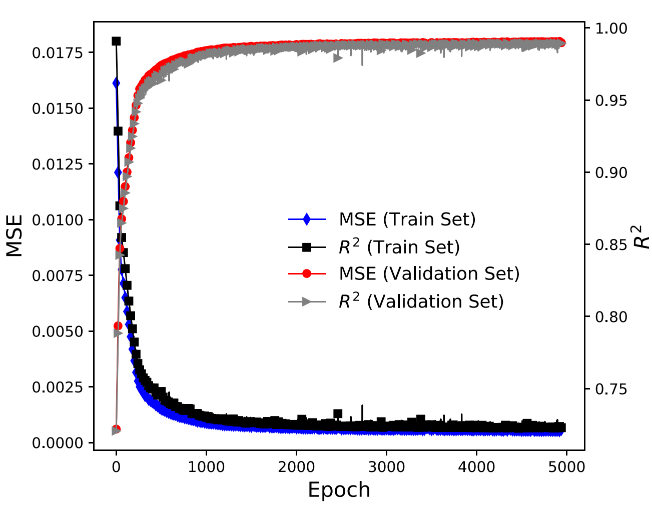

Fig. 30. Variation of R^2 and MSE for the train and validation sets through the training procedure.

6. Wet compression for three classes of axial gas turbines

For estimating operating parameters in inlet fogging and wet compression cooling process, 18 models of gas turbines have been selected. These engines are typically categorized as heavy-duty, industrial, and light-duty gas turbines. Generally, these gas turbines differ about the size, design, and the range of generated power. In this paper, three classes of power outputs are commercial and small industrial units (class A: 1–10 MW), industrial units (class B: 10–80 MW), and heavy-duty units (class C: 80–450 MW). To have a clear insight on the effect of inlet fogging and wet

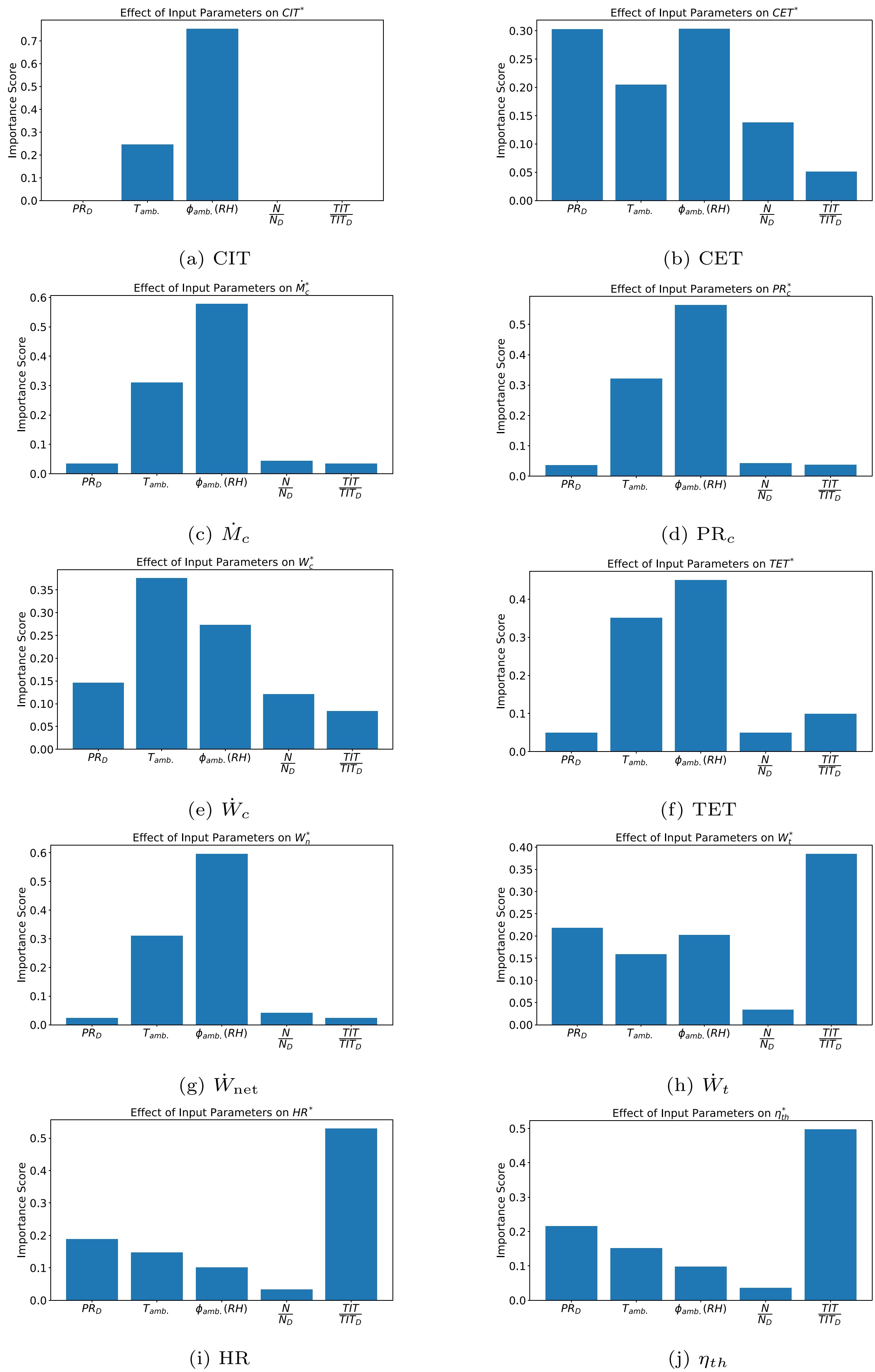

Fig. 31. Results of variable importance analysis (GE9171E).

Table 9
Class A: commercial and small industrial units; computed operating parameters at four off-design conditions.

		CIT	CET	RWI_{SFo}	RWI_{os}	$\dot{M}_c$	$\dot{W}_c$	$\dot{M}_f$	TET	$\dot{W}_t$	$\dot{W}_{net}$	HR	PR_c	η_{th}
		(°C)	(°C)	(kg/s)	(kg/s)	(kg/s)	(MW)	(kg/s)	(∘C)	(MW)	(MW)	(kJ/kWh)		(%)
GT-300	NIC	43.0	419.64	0.0	0.0	26.34	10.42	0.437	564.72	16.56	6.15	12788.11	12.35	28.15
	SFo	30.08	402.24	0.157	0.0	27.63	10.82	0.473	557.36	17.71	6.89	12332.03	12.95	29.19
	OS1% +SFo	30.08	353.3	0.157	0.279	27.89	10.12	0.516	557.65	18.07	7.95	11660.43	13.09	30.87
	OS2% +SFo	30.08	304.41	0.157	0.563	28.14	9.4	0.56	557.76	18.42	9.02	11153.9	13.22	32.28
GT-100	NIC	43.0	407.23	0.0	0.0	17.18	6.56	0.285	566.59	10.54	3.98	12887.88	12.35	27.93
	SFo	30.08	389.96	0.102	0.0	18.02	6.82	0.308	559.4	11.27	4.46	12440.56	12.95	28.94
	OS1% +SFo	30.08	342.82	0.102	0.182	18.19	6.39	0.336	559.62	11.5	5.11	11812.13	13.09	30.48
	OS2% +SFo	30.08	295.79	0.102	0.367	18.35	5.96	0.363	559.67	11.72	5.76	11333.01	13.22	31.77
MGT6100	NIC	43.0	425.66	0.0	0.0	23.08	9.28	0.356	526.48	14.4	5.12	12480.0	12.62	28.85
	SFo	30.08	408.06	0.138	0.0	24.21	9.63	0.385	519.27	15.39	5.76	12022.88	13.23	29.94
	OS1% +SFo	30.08	357.97	0.138	0.244	24.44	8.99	0.423	519.51	15.71	6.72	11313.22	13.37	31.82
	OS2% +SFo	30.08	307.77	0.137	0.493	24.66	8.33	0.462	519.74	16.02	7.7	10791.24	13.5	33.36
M7A-01	NIC	43.0	397.82	0.0	0.0	18.98	7.06	0.313	570.45	11.27	4.21	13381.39	11.47	26.9
	SFo	30.08	380.77	0.113	0.0	19.92	7.33	0.338	563.26	12.05	4.72	12894.82	12.03	27.92
	OS1% +SFo	30.08	336.17	0.113	0.201	20.1	6.92	0.367	563.34	12.29	5.37	12274.46	12.15	29.33
	OS2% +SFo	30.08	291.66	0.113	0.406	20.28	6.49	0.396	563.28	12.53	6.03	11794.59	12.28	30.52
Taurus70	NIC	43.0	413.77	0.0	0.0	23.73	9.23	0.374	516.86	15.15	5.92	11352.9	14.11	31.71
	SFo	30.08	396.12	0.142	0.0	24.9	9.58	0.405	509.84	16.18	6.6	11017.27	14.8	32.68
	OS1% +SFo	30.08	345.9	0.141	0.251	25.12	8.92	0.444	510.16	16.52	7.6	10496.96	14.96	34.3
	OS2% +SFo	30.08	295.73	0.141	0.507	25.35	8.24	0.484	510.45	16.84	8.6	10110.4	15.11	35.61
Saturn20	NIC	43.0	264.49	0.0	0.0	5.64	1.3	0.083	547.69	2.21	0.91	16291.86	5.92	22.1
	SFo	30.08	250.22	0.034	0.0	5.92	1.35	0.089	540.41	2.38	1.02	15640.47	6.2	23.02
	OS1% +SFo	30.08	215.71	0.034	0.06	5.97	1.29	0.096	539.78	2.43	1.13	15138.87	6.27	23.78
	OS2% +SFo	30.08	182.24	0.034	0.121	6.03	1.23	0.102	539.17	2.47	1.24	14784.11	6.33	24.35

Table 10
Class B: industrial units; computed operating parameters at four off-design conditions.

		CIT	CET	RWI_{SFo}	RWI_{os}	$\dot{M}_c$	$\dot{W}_c$	$\dot{M}_f$	TET	$\dot{W}_t$	$\dot{W}_{net}$	HR	PR_c	η_{th}
		(°C)	(°C)	(kg/s)	(kg/s)	(kg/s)	(MW)	(kg/s)	(∘C)	(MW)	(MW)	(kJ/kWh)		(%)
GE6B03	NIC	43.0	357.43	0.0	0.0	127.74	41.95	2.237	570.25	76.41	34.46	11666.07	11.21	30.86
	SFo	30.08	340.92	0.762	0.0	134.02	43.59	2.411	562.83	81.75	38.15	11358.31	11.75	31.69
	OS1% +SFo	30.08	302.33	0.761	1.352	135.25	41.63	2.582	562.67	83.3	41.67	11135.71	11.87	32.33
	OS2% +SFo	30.08	263.84	0.76	2.729	136.46	39.61	2.755	562.48	84.82	45.21	10955.87	11.99	32.86
GT800	NIC	43.0	455.72	0.0	0.0	116.94	50.86	2.178	568.46	88.79	37.93	10319.32	18.0	34.89
	SFo	30.08	437.13	0.698	0.0	122.72	52.71	2.353	561.2	94.71	42.0	10070.43	18.88	35.75
	OS1% +SFo	30.08	375.97	0.697	1.238	123.84	48.07	2.598	562.28	96.78	48.72	9586.12	19.07	37.55
	OS2% +SFo	30.08	315.06	0.696	2.499	124.95	43.32	2.848	563.08	98.78	55.45	9232.99	19.28	38.99
H25	NIC	43.0	451.18	0.0	0.0	100.4	43.17	1.94	592.37	76.17	33.0	10565.97	15.44	34.07
	SFo	30.11	432.92	0.553	0.0	105.34	44.76	2.093	584.65	81.3	36.53	10297.94	16.19	34.96
	OS1% +SFo	30.11	375.39	0.553	1.063	106.3	41.16	2.294	585.41	83.03	41.88	9846.29	16.36	36.56
	OS2% +SFo	30.11	317.86	0.552	2.145	107.25	37.46	2.499	586.01	84.71	47.25	9508.51	16.53	37.86
MGT40	NIC	43.0	381.6	0.0	0.0	129.5	45.89	2.23	570.29	79.06	33.17	12086.59	10.86	29.79
	SFo	30.08	364.8	0.772	0.0	135.87	47.69	2.406	562.7	84.59	36.91	11719.99	11.38	30.72
	OS1% +SFo	30.08	323.42	0.772	1.371	137.11	45.3	2.59	562.54	86.25	40.95	11369.08	11.5	31.66
	OS2% +SFo	30.08	281.97	0.771	2.767	138.35	42.83	2.778	562.41	87.86	45.03	11089.68	11.61	32.46
AE643A	NIC	43.0	422.95	0.0	0.0	189.35	75.58	3.621	576.19	139.75	64.17	10143.82	16.14	35.49
	SFo	30.08	405.0	1.129	0.0	198.69	78.38	3.906	568.7	149.15	70.77	9920.87	16.93	36.29
	OS1% +SFo	30.08	351.02	1.128	2.005	200.5	72.33	4.261	569.4	152.26	79.93	9582.75	17.11	37.57
	OS2% +SFo	30.08	297.33	1.127	4.046	202.3	66.18	4.622	569.86	155.27	89.09	9325.91	17.29	38.6

compression on the operating parameters of various gas turbines, results of simulation in four off-design condition are reported for the aforementioned classes in Tables 9 to 11. The design data of the aforementioned gas turbines are reported in Table 12.

7. Conclusion

This paper presents a developed method for calculating the design and off-design parameters of gas turbine performance based on stage stacking and matching algorithms. Stage stacking through the compressor is conducted with the use of evaluated stage

Table 11
Class C: heavy duty units; computed operating parameters at four off-design conditions.

		CIT	CET	RWI_{SFo}	RWI_{os}	$\dot{M}_c$	$\dot{W}_c$	$\dot{M}_f$	TET	$\dot{W}_t$	$\dot{W}_{net}$	HR	PR_c	η_{th}
		($^\circ C$)	($^\circ C$)	(kg/s)	(kg/s)	(kg/s)	(MW)	(kg/s)	($\circ C$)	(MW)	(MW)	(kJ/kWh)		(%)
MS7001EA	NIC	43.0	372.64	0.0	0.0	257.23	88.68	4.412	562.42	156.1	67.42	11763.2	11.12	30.6
	SFo	30.08	355.99	1.534	0.0	269.89	92.16	4.759	554.86	167.0	74.85	11428.83	11.66	31.5
	OS1% +SFo	30.08	315.39	1.533	2.724	272.36	87.64	5.117	554.78	170.23	82.59	11136.17	11.78	32.33
	OS2% +SFo	30.08	274.87	1.531	5.496	274.81	83.01	5.481	554.63	173.39	90.38	10901.67	11.89	33.02
AE942	NIC	43.0	367.31	0.0	0.0	488.94	165.76	8.797	561.62	313.81	148.06	10680.17	10.59	33.71
	SFo	30.08	350.79	2.916	0.0	512.99	172.3	9.477	553.41	335.85	163.55	10416.33	11.1	34.56
	OS1% +SFo	30.08	311.64	2.913	5.177	517.69	164.47	10.146	553.23	342.26	177.79	10258.01	11.22	35.09
	OS2% +SFo	30.08	272.55	2.91	10.447	522.35	156.43	10.827	552.99	348.54	192.12	10130.44	11.33	35.54
SGT5200E	NIC	43.0	386.44	0.0	0.0	491.54	176.76	8.832	560.15	325.91	149.15	10644.31	11.3	33.82
	SFo	30.08	369.53	2.932	0.0	515.74	183.63	9.522	552.04	348.6	164.97	10375.49	11.84	34.7
	OS1% +SFo	30.08	326.78	2.929	5.205	520.47	173.85	10.25	552.03	355.41	181.56	10148.21	11.96	35.47
	OS2% +SFo	30.08	284.08	2.926	10.503	525.15	163.83	10.992	551.95	362.07	198.24	9967.14	12.08	36.12
M701F	NIC	43.0	486.12	0.0	0.0	658.7	308.49	15.754	654.17	617.4	308.9	9167.75	18.52	39.27
	SFo	30.08	467.12	3.929	0.0	691.22	319.7	16.952	645.54	658.43	338.72	8996.14	19.43	40.02
	OS1% +SFo	30.08	400.52	3.925	6.975	697.51	289.56	18.58	647.05	672.92	383.37	8712.03	19.64	41.32
	OS2% +SFo	30.08	333.86	3.92	14.075	703.74	258.57	20.248	648.28	686.73	428.16	8501.08	19.85	42.35
SGT5800H	NIC	43.0	502.3	0.0	0.0	823.37	400.34	19.153	651.23	764.18	363.84	9462.7	17.65	38.04
	SFo	30.08	483.19	4.912	0.0	864.02	414.97	20.624	642.49	815.19	400.22	9263.08	18.51	38.86
	OS1% +SFo	30.08	414.93	4.907	8.719	871.89	375.72	22.69	644.04	833.37	457.65	8912.15	18.71	40.39
	OS2% +SFo	30.08	346.39	4.901	17.593	879.67	335.19	24.813	645.32	850.69	515.49	8652.58	18.91	41.61
GT26	NIC	43.0	597.48	0.0	0.0	554.68	328.83	12.212	650.33	542.01	213.17	10297.91	28.22	34.96
	SFo	30.08	576.24	3.309	0.0	582.13	340.22	13.207	643.05	577.03	236.81	10025.2	29.59	35.91
	OS1% +SFo	30.08	515.55	3.306	5.874	587.43	318.03	14.46	644.52	589.19	271.17	9586.02	29.92	37.55
	OS2% +SFo	30.08	448.44	3.302	11.853	592.67	291.24	15.857	645.97	601.21	309.97	9195.57	30.25	39.15
GT24	NIC	43.0	592.68	0.0	0.0	360.98	212.04	8.071	647.69	347.47	135.43	10462.0	28.22	34.41
	SFo	30.08	571.5	2.154	0.0	378.85	219.38	8.73	640.51	369.89	150.5	10181.54	29.59	35.36
	OS1% +SFo	30.08	511.33	2.151	3.823	382.29	205.15	9.556	641.94	377.57	172.42	9728.32	29.92	37.01
	OS2% +SFo	30.08	444.91	2.149	7.714	385.7	188.01	10.474	643.37	385.14	197.13	9326.46	30.25	38.6

Table 12
Design parameters of 18 selected gas turbines.

		RPM	PR_c	TET ($^\circ C$)	$\dot{M}$ (kg/s)	$\dot{W}_{net}$ (MW)	HR (kJ/kWh)	Num. Stages
1	SGT-300	14010	14	542	29.9	7.9	10740	10
2	SGT-100	17384	14	545	19.5	5.1	11984	10
3	MGT6100	1500	14.3	505	26.2	6.6	11190	11
4	M7A-01 (GPB60)	14000	13	548	21.55	5.4	12300	12
5	Taurus 70	15200	14	490	26.2	7.52	10650	14
6	Saturn 20	1500	6.7	520	6.4	1.185	14670	8
7	GE 6B.03	5163	12.7	539	145	44	11773	17
8	SGT-800	6608	20.4	553	132.8	47.5	9557	15
9	H-25	7280	17.5	569	92.4	41	9949	17
10	MGT-40	5160	12.3	548	147	42.2	11180	17
11	AE 64.3A	5400	18.3	530	215	80	9890	15
12	MS7001EA (GE 7121)	3600	12.6	537	292	85	10991	17
13	AE 94.2	3000	12	541	555	185	9836	17
14	SGT5-2000E (V94.2)	3000	12.8	536	558	187	9863	16
15	M701F	3000	21	630	748	380	8592	17
16	SGT5-8000H	3000	20	630	935	450	8780	13
17	GT 26	3000	32	615	630	268	9730	22
18	GT 24	3600	32	615	410	171	9863	22

characteristic map and analysis of velocity triangles to accurately calculate load and flow coefficients besides temperature and pressure rise at each stage. Characteristic map of each stage is evaluated using a map zooming technique based on grey wolf optimization (GWO) algorithm. In this regard, the unknown parameters of the characteristic curve of each compressor stage are optimized to minimize the mean-squared error of the overall characteristic map of the compressor with the calculated overall map from the stage stacking. The output results of the modeling are validated using experimental data which is reported in literature and the comparison of results shows an excellent agreement with the mean percentage difference of less than 3%. Unlike evaporative inlet cooling techniques, the wet compression process can be effective at the ambient conditions with high relative humidity. This method leads to an additional mass flow entry to the gas turbine comparing to the dry operating condition. From the results obtained in the present study, it can be seen that the lower portion of the added mass flow rate is directly due to the water spray and most of it is related to the influence of the cooling process and matching of the gas turbine components at a new operation point. The additional power gained by fogging is dependent upon the difference between the ambient dry bulb and wet bulb temperatures. However, the gains by wet compression are more consistent over a wider range of ambient conditions. The amount of water which can be sprayed in the compressor depends on the surge limits for safe and stable compressor operation, blade erosion resistance, and achievable thermal efficiency. As shown in this study, increasing injected water may not improve thermal efficiency, but it leads to a monotonic increase of the net power output. The effects of the ambient conditions, the amount of water injection, and the presence and evaporation of water droplets on the gas turbine operating parameters are studied. The most important parameters for industrial stationary gas turbine users are the variation of the net output power and thermal efficiency. The quantitative results are presented for these two important parameters for the five cities where cooling systems can be installed in different weather conditions. It is observed that, in higher ambient temperatures with lower relative humidity, fogging and wet compression processes are more effective. With the increase of the ambient relative humidity, the effect of saturated fogging is diminished where operating points related to the saturated fogging condition move towards the dry operating points. The developed technique based on the variable importance (VI) by constructing and training an artificial neural network (ANN) is implemented for sensitivity analysis of the wet compression process. Results show that the influence of ambient relative humidity and ambient temperature on the net power output change due to the wet compression process are dominant. However, the thermal efficiency change due to the wet compression is more sensitive to the turbine inlet temperature (TIT) variations.

CRediT authorship contribution statement

Mirhamed Salehi: Data curation, Writing - original draft, preparation, Software. **Hamidreza Eivazi:** Data curation, Writing - original draft, preparation, Software. **Mojtaba Tahani:** Conceptualization, Methodology, Validation, Project administration, Reviewing and Editing, Investigation. **Mehran Masdari:** Supervision.

Declaration of competing interest

The authors declare that they have no known competing financial interests or personal relationships that could have appeared to influence the work reported in this paper.

Appendix

Grey Wolf Optimization Algorithm

The Grey Wolf Optimizer (GWO) is a nature inspired meta-heuristic algorithm. The mathematical model of this optimizer was developed based on the leadership hierarchy and hunting behavior of the grey wolves. The social dominant hierarchy is shown in Fig. 32, which is adapted from the original paper (Mirjalili et al., 2014).

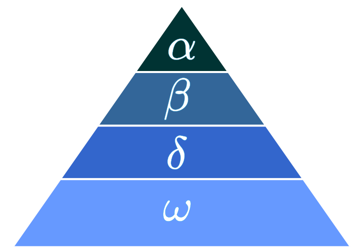

Fig. 32. Hierarchy of grey wolf (dominance decreases from top down) (Mirjalili et al., 2014).

The main phases of grey wolf hunting are as follows:

- Tracking, chasing, and approaching the prey.
- Pursuing, encircling, and harassing the prey until it stops moving.
- Attack towards the prey.

In order to mathematically model encircling behavior the following equations are proposed (Mirjalili et al., 2014):

$$\vec{D} = \left|\vec{C}\vec{\mathscr{X}}_p(t) - \vec{\mathscr{X}}(t)\right|, \vec{\mathscr{X}}(t+1) = \vec{\mathscr{X}}(t) - \vec{A}\cdot\vec{D}. \quad (27)$$

where t indicates the current iteration, $\vec{A}$ and $\vec{C}$ are coefficient vectors, $\vec{\mathscr{X}}_p$ is the position vector of the prey, and $\vec{\mathscr{X}}$ indicates the position vector of a grey wolf. The vectors $\vec{A}$ and $\vec{C}$ are calculated as follows:

$$\vec{A} = 2\vec{a}\cdot\vec{r_1} - \vec{a}, \vec{C} = 2\vec{r_2}, \quad (28)$$

where $\vec{a}$ is components of are linearly decreased from 2 to 0 over the course of iterations and $\vec{r_1}$ and $\vec{r_1}$ are random vectors in [0, 1]. Grey wolves have the ability to recognize the location of prey and encircle them. The hunt is usually guided by the alpha. The beta and delta might also participate in hunting occasionally. alpha (best candidate solution) beta, and delta know the knowledge of the potential location of prey. So, in mathematical simulation this knowledge is assumed as solution candidate.

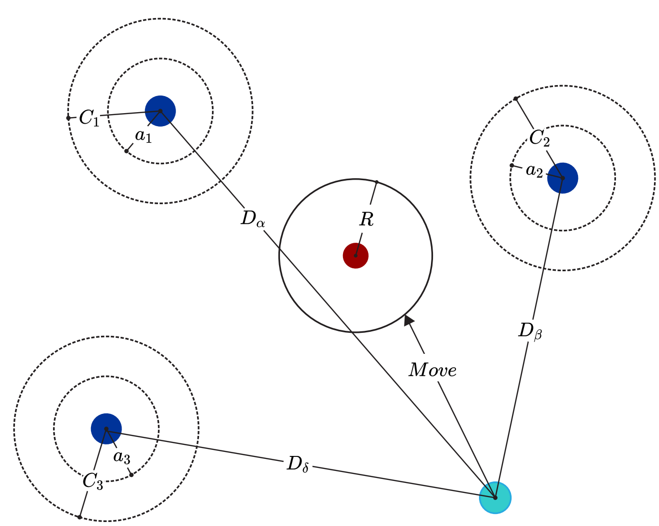

Fig. 33. Position updating in GWO (Mirjalili et al., 2014).

Fig. 33 (Mirjalili et al., 2014) shows how a search agent updates its position according to alpha, beta, and delta in a 2D search space. It can be observed that the final position would be in a random place within a circle which is defined by the positions of alpha, beta, and delta in the search space. The algorithmic steps of Grey Wolf Optimizer (GWO) may be summarized as below (Guha et al., 2016):

1. The search process is started with random initialization of candidate solutions (wolves) in the search space.
2. Alpha, beta and delta wolves are estimated based on the position of prey.
3. To find the optimum location of prey, each wolf updates its position.
4. A control parameter $\overrightarrow{a}$ linearly decreases from 2 to 0 for better exploitation and exploration of candidate solutions
5. Candidate solutions tend to diverge when $\overrightarrow{A} > 1$ and to converge when $\overrightarrow{A} < 1$ and at the end GWO gives the optimum solution.

General algorithm of Grey Wolf Optimizer (GWO) is shown Fig. 34.

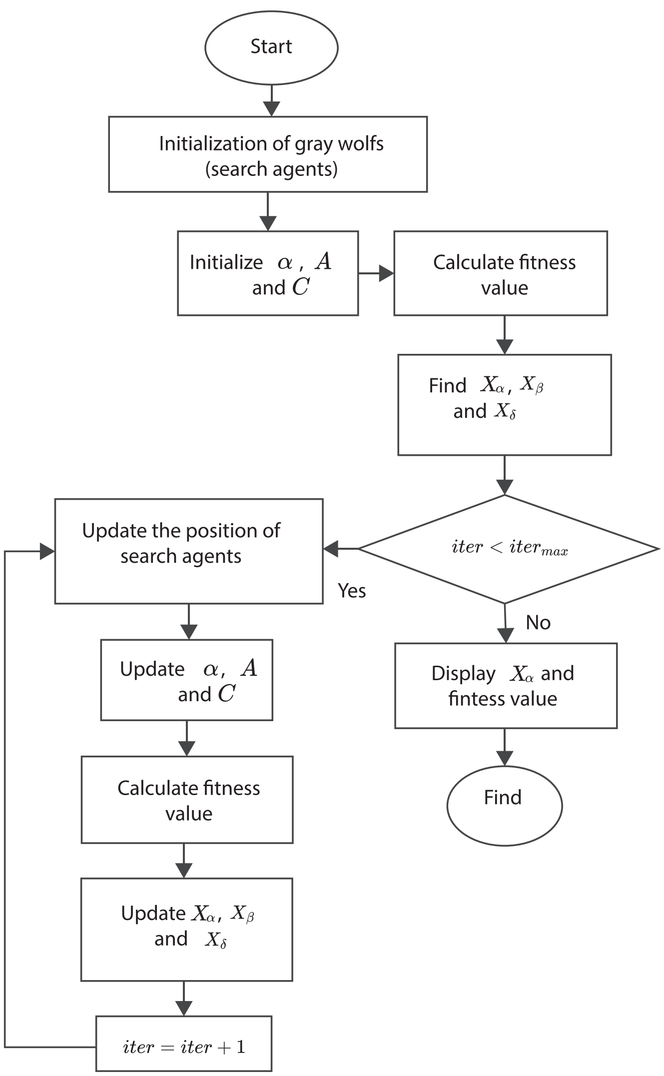

Fig. 34. Flowchart of grey wolf optimization algorithm (Guha et al., 2016).

References

Al-Ibrahim, A.M., Varnham, A., 2010. A review of inlet air-cooling technologies for enhancing the performance of combustion turbines in Saudi Arabia. Appl. Therm. Eng. 30 (14), 1879–1888.

Bagnoli, M., Bianchi, M., Melino, F., Spina, P.R., 01 2008. Development and validation of a computational code for wet compression simulation of gas turbines. J. Eng. Gas Turbines Power 130 (1), 012004.

Bhargava, R., Meher-Homji, C.B., 02 2005. Parametric analysis of existing gas turbines with inlet evaporative and overspray fogging. J. Eng. Gas Turbines Power 127 (1), 145–158.

Breiman, L., Oct 2001. Random forests. Mach. Learn. 45 (1), 5–32.

Cataldi, G., Guntner, H., Matz, C., McKay, T., Hoffmann, J., Nemet, A., Lecheler, S., Braun, J., 03 2006. Influence of high fogging systems on gas turbine engine operation and performance. J. Eng. Gas Turbines Power 128 (1), 135–143.

Cerri, G., Salvini, C., Procacci, R., Rispoli, F., 05 1993. Fouling and air bleed extracted flow influence on compressor performance. In: ASME 1993 International Gas Turbine and Aeroengine Congress and Exposition (GT1993). Vol. Volume 3C: General. V03CT17A027.

Chaker, M., Mee, Thomas R., 06 2015. Design consideration of fogging and wet compression systems as function of gas turbine inlet duct configurations. In: ASME Turbo Expo 2015: Turbine Technical Conference and Exposition (GT2015). Vol. Volume 3: Coal, Biomass and Alternative Fuels; Cycle Innovations; Electric Power; Industrial and Cogeneration. V003T20A015.

Chaker, M., Meher-Homji, C.B., Mee, T., 06 2002. Inlet fogging of gas turbine engines: Part A – fog droplet thermodynamics, heat transfer and practical considerations. In: ASME Turbo Expo 2002: Power for Land, Sea, and Air (GT2002). Vol. Volume 4: Turbo Expo 2002, Parts A and B, pp. 413–428.

Chaker, M., Meher-Homji, C.B., Mee, T., 06 2003. Inlet fogging of gas turbine engines: experimental and analytical investigations on impaction pin fog nozzle behavior. In: ASME Turbo Expo 2003, Collocated with the 2003 International Joint Power Generation Conference (GT2003). Vol. Volume 2: Turbo Expo 2003, pp. 863–879.

Ehyaei, M.A., Tahani, M., Ahmadi, P., Esfandiari, M., feb 2015. Optimization of fog inlet air cooling system for combined cycle power plants using genetic algorithm. Appl. Therm. Eng. 76, 449–461.

Eivazi, H., Guastoni, L., Schlatter, P., Azizpour, H., Vinuesa, R., 2020. Recurrent Neural Networks and Koopman-Based Frameworks for Temporal Predictions in Turbulence.

Fisher, A., Rudin, C., Dominici, F., 2018. All Models Are Wrong, but Many Are Useful: Learning a Variable's Importance by Studying an Entire Class of Prediction Models Simultaneously.

Guha, D., Roy, P.K., Banerjee, S., 2016. Load frequency control of large scale power system using quasi-oppositional grey wolf optimization algorithm. Eng. Sci. Technol. Int. J. 19 (4), 1693–1713.

Hamrick, J.T., Beede, W.L., 1956. Some investigations with wet compression. Trans. ASME 2, 409–420.

Hendricks, R., Shouse, D., Roquemore, W., 2005. Water injected turbomachinery. In: NASA Technical Report. NASA/TM–2005-212632.

Hill, P.G., nov 1963. Aerodynamic and thermodynamic effects of coolant injection on axial compressors. Aeronaut. Q. 14 (4), 331–348.

Howell, A.R., Bonham, R.P., jun 1950. Overall and stage characteristics of axial-flow compressors. Proc. Inst. Mech. Eng. 163 (1), 235–248.

Kanbur, B.B., Xiang, L., Dubey, S., Choo, F.H., Duan, F., 2018. Life cycle-based enviroeconomic and thermal analyses of the inlet air-cooled microturbine systems with liquefied natural gas cold energy. J. Clean. Prod. 174, 1338–1350.

Khan, J., Wang, T., 06 2008. Simulation of inlet fogging and wet-compression in a single stage compressor including erosion analysis. In: ASME Turbo Expo 2008: Power for Land, Sea, and Air (GT2008). Vol. Volume 7: Education; Industrial and Cogeneration; Marine; Oil and Gas Applications, pp. 193–206.

Khan, J.R., Wang, T., jan 2006. Fog and overspray cooling for gas turbine systems with low calorific value fuels. In: ASME Turbo Expo 2006: Power for Land, Sea, and Air (GT2006). Vol. Volume 4: Cycle Innovations; Electric Power; Industrial and Cogeneration; Manufacturing Materials and Metallurgy, pp. 669–682.

Khan, J.R., Wang, T., 06 2009. Overspray fog cooling in compressor using stage-stacking scheme with non-equilibrium heat transfer model for droplet evaporation. In: ASME Turbo Expo 2009: Power for Land, Sea, and Air (GT2009). Vol. Volume 4: Cycle Innovations; Industrial and Cogeneration; Manufacturing Materials and Metallurgy; Marine, pp. 609–622.

Khoshroo, A., Emrouznejad, A., Ghaffarizadeh, A., Kasraei, M., Omid, M., 2018. Sensitivity analysis of energy inputs in crop production using artificial neural networks. J. Clean. Prod. 197, 992–998.

Kingma, D., Ba, J., 2015. Adam: a method for stochastic optimization. In: Proceedings of the 3rd International Conference for Learning Representations (Iclr'15). San Diego.

Lee, B.I., Kesler, M.G., 1975. A generalized thermodynamic correlation based on three-parameter corresponding states. AIChE J. 21 (3), 510–527.

Liu, C., Zheng, Q., Wang, Q., Lin, A., Jiang, Y., Luo, M., 2019. Sensitivity analysis of multistage compressor characteristics under the spray atomization effect using a CFD model. Energies 12 (2).

MAPNA, 03 2018. Design and implementation of wet compression system for MGT-70 fleet. In: Technical Review. MAPNA Turbine Engineering and Manufacturing CO. (TUGA), pp. 11–19. http://ttc.mapnaturbine.com/Portals/1/Users/080/80/80/Paper-NO.21.pdf.

Matz, C., Cataldi, G., Kappis, W., Mundinger, G., Bischoff, S., Helland, E., Ripken, M., oct, 2010. Prediction of evaporative effects within the blading of an industrial axial compressor. J. Turbomach. 132 (4), 041013.

MeeFog, 2015. Gas turbine inlet air cooling and wet compression. In: Technical Report. Mee Industries Inc., California. https://www.meefog.com/wp-content/uploads/br-gt-gasturbine.pdf.

Mertens, J., Prieur-Vernat, A., Corbisier, D., Favrot, E., Boon, G., 2015. Water footprinting of electricity generated by combined cycle gas turbines using different cooling technologies: a practitioner's experience. J. Clean. Prod. 86, 201–208.

Mirjalili, S., Mirjalili, S.M., Lewis, A., mar, 2014. Grey wolf optimizer. Adv. Eng. Software 69, 46–61.
Mohan, A., Chidambaram, P.K., Suryan, A., Kim, H.D., 2019. Energy efficiency analysis of wet compression systems through thermo-fluid dynamic considerations. J. Clean. Prod. 214, 132–144.
Muir, D.E., Saravanamuttoo, H.I.H., Marshall, D.J., 04 1989. Health monitoring of variable geometry gas turbines for the canadian navy. J. Eng. Gas Turbines Power 111 (2), 244–250.
Novelo, D.A.B., Igie, U., Prakash, V., Szymański, A., 2019. Experimental investigation of gas turbine compressor water injection for nox emission reductions. Energy 176, 235–248.
Obermüller, M., Schmidt, K., Schulte, H., Peitsch, D., 2012. Some Aspects on Wet Compression-Physical Effects and Modeling Strategies Used in Engine Performance Tools. Deutsche Gesellschaft für Luft-und Raumfahrt-Lilienthal-Oberth eV. Sept. 10-12, Paper No. DLRK-2012-281210.
Roumeliotis, I., Mathioudakis, K., 03 2004. Evaluation of interstage water injection effect on compressor and engine performance. J. Eng. Gas Turbines Power 128 (4), 849–856.
Roumeliotis, I., Mathioudakis, K., 2010. Evaluation of water injection effect on compressor and engine performance and operability. Appl. Energy 87 (4), 1207–1216.
Sahu, M.K., Sanjay, 2018. Thermoeconomic investigation of basic and intercooled gas turbine based power utilities incorporating air-film blade cooling. J. Clean. Prod. 170, 842–856.
Sanaye, S., Rezazadeh, H., Aghazeynali, M., Samadi, M., Mehranian, D., Ahangaran, M.K., 05 2006. Effects of inlet fogging and wet compression on gas turbine performance. In: ASME Turbo Expo 2006: Power for Land, Sea, and Air (GT2006). Vol. Volume 4: Cycle Innovations; Electric Power; Industrial and Cogeneration; Manufacturing Materials and Metallurgy, pp. 769–776.
Sanjay, 2011. Investigation of effect of variation of cycle parameters on thermodynamic performance of gas-steam combined cycle. Energy 36 (1), 157–167.
Saravanamuttoo, H.I.H., Rogers, G.F.C., Cohen, H., 2001. Gas Turbine Theory. Pearson Education.
Sexton, M.R., Urbach, H.B., Knauss, D.T., 06 1998. Evaporative compressor cooling for NOx suppression and enhanced engine performance for naval gas turbine propulsion plants. In: ASME 1998 International Gas Turbine and Aeroengine Congress and Exhibition (GT1998). Vol. Volume 2: Aircraft Engine; Marine; Microturbines and Small Turbomachinery. V002T03A015.
Sexton, W.R., Sexton, M.R., 06 2003. The effects of wet compression on gas turbine engine operating performance. In: ASME Turbo Expo 2003, Collocated with the 2003 International Joint Power Generation Conference (GT2003). Vol. Volume 2: Turbo Expo 2003, pp. 673–679.
Shin, Y., Kim, Z., Yu, J., Kim, G., Hwang, S., 2019. Development of NOx reduction system utilizing artificial neural network (ANN) and genetic algorithm (GA). J. Clean. Prod. 232, 1418–1429.
Siemens, 2013. Gas turbine wet compression modernization. In: Technical Report. Siemens AG Energy Sector. https://assets.new.siemens.com/siemens/assets/public.1541967401.8d84dc674a1eaec0f133f0bea9079ccf1ceab3bd.wet_compression_e50001-g520-a156-v2-4a00enhrfinal.pdf.
Spina, P.R., 06 2002. Gas turbine performance prediction by using generalized performance curves of compressor and turbine stages. In: ASME Turbo Expo 2002: Power for Land, Sea, and Air (GT2002). Vol. Volume 2: Turbo Expo 2002, Parts A and B, pp. 1073–1082.
Tahani, M., Masdari, M., Salehi, M., Ahmadi, N., oct 2018. Optimization of wet compression effect on the performance of V94.2 gas turbine. Appl. Therm. Eng. 143, 955–963.
Tsalavoutas, A., Stamatis, A., Mathioudakis, K., 06 1994. Derivation of compressor stage characteristics, for accurate overall performance map prediction. In: ASME 1994 International Gas Turbine and Aeroengine Congress and Exposition (GT1994). Vol. Volume 5: Manufacturing Materials and Metallurgy; Ceramics; Structures and Dynamics; Controls, Diagnostics and Instrumentation; Education; General. V005T15A019.
Utamura, M., Kuwahara, T., Murata, H., Horii, N., 07 1999. Effects of intensive evaporative cooling on performance characteristics of land-based gas turbine. In: Proceedings ASME Joint Power Generation Conference, pp. 321–328.
Wang, T., Khan, J.R., 06 2008. Overspray and interstage fog cooling in compressor using stage-stacking scheme: Part 1—development of theory and algorithm. In: Volume 7: Education; Industrial and Cogeneration; Marine; Oil and Gas Applications, pp. 99–109.
WeatherAtlas, 2002-2020. Weather forecast and climate information for cities all over the globe. https://www.weather-atlas.com/en/.
White, A.J., Meacock, A.J., 11 2004. An evaluation of the effects of water injection on compressor performance. J. Eng. Gas Turbines Power 126 (4), 748–754.
White, A.J., Meacock, A.J., 04 2011. Wet compression analysis including velocity slip effects. J. Eng. Gas Turbines Power 133 (8), 081701.
Zeiler, M.D., 2012. ADADELTA: an Adaptive Learning Rate Method.
Zheng, Q., Li, M., Sun, Y., 06 2003. Thermodynamic performance of wet compression and regenerative (WCR) gas turbine. In: ASME Turbo Expo 2003, Collocated with the 2003 International Joint Power Generation Conference (GT2003). Vol. Volume 2: Turbo Expo 2003, pp. 813–820.
Zheng, Q., Sun, Y., Li, S., Wang, Y., 06 2002. Thermodynamic analyses of wet compression process in the compressor of gas turbine. In: ASME Turbo Expo 2002: Power for Land, Sea, and Air (GT2002). Vol. Volume 4: Turbo Expo 2002, Parts A and B, pp. 487–496.
Zurigat, Y.H., Dawoud, B., Bortmany, J., 2006. On the technical feasibility of gas turbine inlet air cooling utilizing thermal energy storage. Int. J. Energy Res. 30 (5), 291–305.